

Skewed Distributions and Opposite Velocity Gradients of Submillimeter Molecular Lines in Low-Mass Protostellar Envelopes

Shigehisa TAKAKUWA

Academia Sinica Institute of Astronomy and Astrophysics, P.O. Box 23-141, Taipei 10617, Taiwan
takakuwa@asiaa.sinica.edu.tw

and

Takeshi KAMAZAKI

Joint ALMA Observatory, Av. Alonso de Cordova 3107, Vitacura, Santiago, Chile
tkamazaki@alma.cl

(Received 2010 November 18; accepted 2011 May 8)

Abstract

We have made mapping observations of L1551 IRS 5, L1551NE, L723, and L43 and single-point observations of IRAS 16293-2422 in the submillimeter CS ($J = 7-6$) and HCN ($J = 4-3$) lines with ASTE. Including our previous ASTE observations of L483 and B335, we found a clear linear correlation between the source bolometric luminosities and the total integrated intensities of the submillimeter lines ($I_{CS} \propto L_{bol}^{0.92}$). The combined ASTE + SMA CS (7-6) image of L1551 IRS 5 exhibits an extended (~ 2000 AU) component tracing the associated reflection nebula at the west and southwest, as well as a compact ($\lesssim 500$ AU) component centered on the protostellar position. The emission peaks of the CS and HCN emissions in L1551 NE are not located at the protostellar position but offset (~ 1400 AU) toward the associated reflection nebula at the west. With the statistical analyses, we confirmed the opposite velocity gradients of the CS (7-6) emission to those of the millimeter lines along the outflow direction, which we reported in our early paper. The magnitudes of the submillimeter velocity gradients are estimated to be $(9.7 \pm 1.7) \times 10^{-3} \text{ km s}^{-1} \text{ arcsec}^{-1}$ in L1551 IRS 5 and $(7.6 \pm 2.4) \times 10^{-3} \text{ km s}^{-1} \text{ arcsec}^{-1}$ in L483. We suggest that the “skewed” submillimeter molecular emissions toward the associated reflection nebulae at a few thousands AU scale trace the warm ($\gtrsim 40$ K) walls of the envelope cavities, excavated by the associated outflows and irradiated by the central protostars directly. The opposite velocity gradients along the outflow direction likely reflect the dispersing gas motion at the wall of the cavity in the envelopes perpendicular to the outflow.

Key words: ISM: molecules – ISM: structure – submillimeter – stars: formation

1. Introduction

Low-mass stars form in 3000 - 10000 AU scale condensations of molecular gas and dusts, so-called dense cores (André et al. 2000; Myers et al. 2000). Previous interferometric observations in millimeter molecular lines have revealed rotating and infalling gas motions in dense cores associated with protostars, “protostellar envelopes” (Ohashi et al. 1996; Ohashi et al. 1997a; Ohashi et al. 1997b; Momose et al. 1998). These millimeter observations have probed structures and kinematics of molecular gas with a temperature of $\sim 10 - 20$ K and a density of 10^{4-6} cm^{-3} in the envelopes. On the other hand, submillimeter molecular lines can trace warmer ($\gtrsim 40$ K) and denser ($\gtrsim 10^7 \text{ cm}^{-3}$) regions, and recent interferometric observations of protostellar envelopes in submillimeter molecular lines with the SMA have revealed compact ($\lesssim 500$ AU) components associated with the central protostars, which often show rotational (possibly Keplerian) gas motion around the protostars (Takakuwa et al. 2004; Takakuwa et al. 2007b; Brinch et al. 2007; Lommen et al. 2008; Jørgensen et al. 2009; Yen, Takakuwa, & Ohashi 2011).

The SMA observations of protostellar envelopes, however, suffer from the effect of the missing flux. For example, the SMA observations of L1551 IRS 5 in the CS ($J = 7-6$) line (Takakuwa et al. 2004) and those of IRAS 16293-2422 in the HCN ($J = 4-3$) line (Takakuwa et al. 2007b) recovered only ~ 11 % and ~ 35 % of the total fluxes observed with CSO and JCMT, respectively, suggesting the presence of the extended ($\gtrsim 2000$ AU) submillimeter components. In fact, the combined SMA + JCMT image of IRAS 16293-2422 in the HCN ($4-3$) line shows an extended (~ 3000 AU) envelope structure as well as a compact (~ 500 AU) disklike structure associated with the protostar. These results suggest that there is extended ($\gtrsim 2000$ AU), warm ($\gtrsim 40$ K) and/or dense ($\gtrsim 10^7 \text{ cm}^{-3}$) gas in protostellar envelopes.

In order to investigate the origin of the extended submillimeter molecular emissions in protostellar envelopes, we initiated mapping observations of protostellar envelopes in the CS ($7-6$) and HCN ($4-3$) lines with Atacama Submillimeter Telescope Experiment (ASTE)¹, a 10-m submillimeter single-dish telescope at the Atacama Site in Chile (Takakuwa et al. 2007a; hereafter Paper I). In Paper I, we mapped the protostellar envelopes around L483 and B335. In L483, the HCN emission is slightly resolved and exhibits a western extension (~ 5000 AU) toward the direction of the associated reflection nebula and the blueshifted outflow. Furthermore,

¹ The ASTE project is driven by Nobeyama Radio Observatory (NRO), a branch of National Astronomical Observatory of Japan (NAOJ), in collaboration with University of Chile, and Japanese institutes including University of Tokyo, Nagoya University, Osaka Prefecture University, Ibaraki University., and Hokkaido University.

the position-velocity diagrams of the HCN and CS emissions along the axis of the associated molecular outflows in L483 and B335 exhibit possible velocity gradients opposite to those of the millimeter emissions or the associated molecular outflows.

These results in Paper I are, however, still a little marginal and more robust confirmations of those results, including more observing samples and more sophisticated data analyses, are required. In the present paper, we have expanded our previous ASTE observations and have performed mapping observations of L1551 IRS 5, L1551 NE, L723, and L43. All of these and previous source samples are nearby ($D \lesssim 300$ pc) and representative ($L_{bol} \gtrsim 3 L_{\odot}$) low-mass protostellar objects suitable for the purpose of the present study. We have constructed data analysis tools by ourselves and have performed more objective, unambiguous data analyses of the previous and the present new data. From these observations and data analyses, we have revealed that the submillimeter molecular lines often show “skewed” emission distributions tracing the reflection nebula (L1551 IRS 5, L483, L1551 NE, and L723), and have found a linear correlation between the intensity of the submillimeter molecular lines and the protostellar luminosities. We have also verified the presence of the opposite velocity gradients of the submillimeter CS line to those of the millimeter lines and the associated outflows in L1551 IRS 5 and L483. With these results obtained from our ASTE observations and data analyses, we discuss the origin of the submillimeter molecular emissions in low-mass protostellar envelopes.

The structure of the present paper is as follows. In §2, we describe our new ASTE observations, and combination of the ASTE CS (7–6) data with the previously-published SMA CS (7–6) data in L1551 IRS 5 (Takakuwa et al. 2004). In §3.1., we discuss all the observed spectra toward the protostellar positions, while in §3.2. we show the new results of the mapping observations. In §4.1., we discuss the extents and distributions of the submillimeter molecular lines and their origin, including our simple radiative-transfer model. In §4.2., we verify the presence of the opposite velocity gradients with our statistical analyses, and discuss a possible reason for the opposite submillimeter velocity gradients.

2. ASTE Observations and Combining with the SMA Data

With the ASTE 10-m telescope we made mapping observations of L1551 IRS 5, L1551 NE, L723, and L43, in the CS ($J = 7-6$; 342.882866 GHz) and HCN ($J = 4-3$; 354.505480 GHz) lines on 2006 August 26, 28 – September 2. Remote observations were performed from an ASTE operation room of NAOJ at Mitaka, Japan, using the network observation system N-COSMOS3 developed by NAOJ (Kamazaki et al. 2005). Details of the ASTE telescope are presented by Ezawa et al. (2004). A cartridge-type 350 GHz receiver mounted on ASTE is a double sideband instrument with an IF frequency range of 5 to 7 GHz (Kohno 2005), and the CS and HCN lines were observed simultaneously at different sidebands. The telescope beam size and the spectral resolution were $\sim 22''$ and 125 kHz (~ 0.11 km s $^{-1}$), respectively. The typical DSB system noise temperature was $\sim 270 - 500$ K. The telescope pointing was checked at

the beginning and the middle of the observations by making continuum observations of Uranus or Jupiter, or five-point CO ($J = 3-2$) observations of a late-type star, O-Cet, and was found to be better than $2''$ during the whole observing period.

As a standard source we also observed the central positions of IRAS 16293-2422 and L1551 IRS 5, and confirmed that the relative intensity was consistent within $\sim 30\%$. The total on-source integration times for IRAS 16293-2422 and L1551 IRS 5 were 11.8 minutes and 23.8 minutes, respectively. We compared the observed CS and HCN spectra toward IRAS 16293-2422 to those obtained with the CSO telescope which has the same dish size as that of the ASTE telescope (Blake et al. 1994; van Dishoeck et al. 1995), and found that the main beam efficiency of ASTE was ~ 0.6 both for the CS and HCN lines. No further correction for the sideband ratio was performed. Hereafter we show the observed line intensities in the unit of T_{MB} .

In the mapping observations, typical rms noise levels per point were ~ 0.16 K, ~ 0.20 K, ~ 0.20 K, and ~ 0.27 K in L1551 IRS 5, L1551 NE, L723, and L43, respectively, with a typical on-source integration time of $\sim 4 - 12$ minutes. The mapping regions cover most of the CS and HCN emission regions at a grid spacing of $10''$, providing the Nyquist-sampled maps. Toward the center of L43 a better rms noise level (~ 0.18 K) was obtained with an on-source integration time of 13.3 minutes, to compare the central spectra to those toward other sources. In Paper I, we performed mapping observations of L483, B335, and single-point observations of L723 and IRAS 16293-2422, and in total we observed seven protostellar sources in the submillimeter CS and HCN lines with ASTE. The observed source properties and the ASTE observations from Paper I and the present paper (hereafter Paper II) are summarized in Table 1. Figure 1 shows the CS and HCN spectra toward IRAS 16293-2422 after combining both the Paper I and II data, and Figure 2 shows the observed CS ($J = 7-6$) and HCN ($J = 4-3$) spectra toward the central positions of all the other protostellar sources.

We also combined the ASTE CS (7-6) image of L1551 IRS 5 with the SMA CS (7-6) image (Takakuwa et al. 2004), adopting the method described by Takakuwa et al. (2007b). Details of the SMA observations are described in Takakuwa et al. (2004). The conversion factor from T_{MB} (K) to S (Jy beam^{-1}) was derived to be 46.6 as

$$S = \frac{2k_B\Omega_{beam}}{\lambda^2}T_{MB}, \quad (1)$$

where k_B is the Boltzmann constant, λ is the wavelength, and Ω_{beam} is the solid angle of the ASTE beam ($= 22''$). The SMA observations recovered $\sim 10\%$ of the total CS (7-6) flux observed with ASTE. The resultant synthesized beam size and the rms noise level per channel in the combined image are $3''.6 \times 2''.7$ (P.A. = -65°) and ~ 1.1 Jy beam^{-1} , respectively, where the velocity resolution is the same as that of the SMA data (~ 0.179 km s^{-1}).

Table 1. Observed sources

Source	IRAS	L_{bol} (L_{\odot})	T_{bol} (K)	R. A. (J2000.0)	Dec. (J2000.0)	Distance (pc)	Ref. *	ASTE Observation
L1551 IRS 5	04287+1801	22	92	04 ^h 31 ^m 34 ^s .14	18°08′05″.1	140	1,2,3,4	Paper II (mapping)
L1551 NE	04289+1802	4.2	91	04 31 44.47	18 08 32.2	140	1,2,4,5	Paper II (mapping)
IRAS 16293-2422	16293-2422	21	42	16 32 22.87	-24 28 36.6	160	2,6,7	Paper I & II (both one point)
L43	16316-1540	2.7	370	16 34 29.30	-15 47 01.7	125	8,9	Paper II (mapping)
L483	18148-0440	13	52	18 17 29.86	-04 39 38.7	200	2,8,10	Paper I (mapping)
L723	19156+1906	3.3	47	19 17 53.62	19 12 19.5	300	2,8,11	Paper I (one point) & II (mapping)
B335	19345+0727	3.1	28	19 37 00.94	07 34 08.8	150	2,8,12	Paper I (mapping)

* (1) Emerson et al. 1984; (2) Froebrich 2005; (3) Takakuwa et al. 2004; (4) Saito et al. 2001; (5) Moriarty-Schieven et al. 2000; (6) Gregersen et al. 1997; (7) Takakuwa et al. 2007b; (8) Shirley et al. 2000; (9) Chen et al. 2009; (10) Park et al. 2000; (11) Anglada et al. 1991; (12) Yen, Takakuwa, & Ohashi 2010a

3. Results

3.1. Submillimeter CS and HCN Spectra

Figures 1 and 2 show the observed ASTE CS ($J = 7-6$) and HCN ($J = 4-3$) spectra toward the protostellar positions of all of our targets, and Table 2 summarizes the observed line parameters derived from Gaussian fittings unless otherwise noted. Except for the CS and HCN lines toward L1551 NE and the CS line toward L43, we detected these submillimeter lines above 4σ level. The CS line is stronger than the HCN line except for L43. The CS intensity ranges from $\lesssim 0.5$ K (L1551 NE) to ~ 9.1 K (IRAS 16293-2422) and the HCN intensity from ~ 0.4 K (L723) to ~ 5.8 K (IRAS 16293-2422). The line widths of these lines are typically $\sim 1 - 2$ km s⁻¹. Toward L483 and L723 the HCN line widths are significantly wider than the CS line widths. The HCN ($J = 4-3$) line consists of six hyperfine components, two of which ($F = 3-3$ and $4-4$) can be separated from the main line ($F = 4-3$) by 1.977 MHz (-1.67 km s⁻¹) and -1.610 MHz (1.36 km s⁻¹), respectively (Jewitt et al. 1997). The intensity ratio between the main and the other two hyperfine lines at the local thermal equilibrium condition is 0.0217 (Jewitt et al. 1997), and these weaker hyperfine lines are unlikely to be detectable with the present observations. It is still possible, however, that the broader HCN line widths than the CS line widths found in L483 and L723 are due to the presence of the hyperfine lines, if there is any hyperfine anomaly.

Toward L1551 IRS 5 ($L_{bol} = 22 L_{\odot}$) and L483 ($L_{bol} = 13 L_{\odot}$), the submillimeter intensities are \sim twice as high as those toward the other, less bright ($L_{bol} \lesssim 4.2 L_{\odot}$) sources, with an exception of the CS line toward B335 and the HCN line toward L43. Toward IRAS 16293-2422 ($L_{bol} = 21 L_{\odot}$) the submillimeter CS and HCN intensities are much stronger than those toward the other sources (Fig. 1). These results suggest that the intensities of the submillimeter

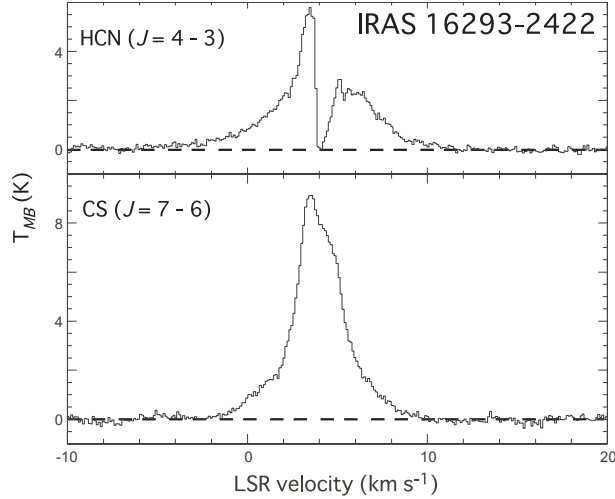


Fig. 1. CS ($J = 7-6$) and HCN ($J = 4-3$) spectra toward IRAS 16293-2422 observed with ASTE.

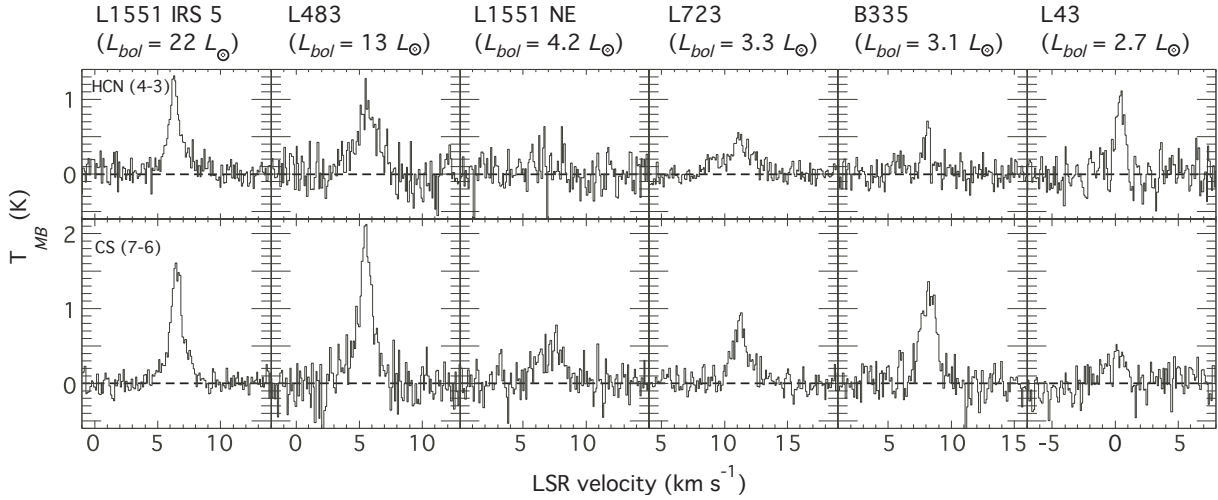


Fig. 2. CS ($J = 7-6$) (*lower*) and HCN ($J = 4-3$) (*upper*) spectra toward the protostellar positions, observed with ASTE.

molecular lines are related to the protostellar luminosities. We will discuss this point in §4.1.

3.2. Distribution of the Submillimeter CS and HCN Emission

3.2.1. L1551 IRS 5

L1551 IRS 5 is the brightest ($\sim 22 L_{\odot}$) protostellar source in Taurus, and is classified as Class I (Emerson et al. 1984; Froebrich 2005). L1551 IRS 5 was the first protostellar source where a bipolar molecular outflow was identified (Snell et al. 1980). Subsequent observations of L1551 IRS 5 in CO (1–0, 2–1, 3–2) lines have revealed structures and kinematics of the parsec-scale molecular outflow, with the blueshifted and redshifted lobes at the south-west and north-east of the protostar, respectively (Uchida et al. 1987; Stojimirović et al. 2006; Moriarty-Schieven et al. 2006). High angular-resolution ($\sim 0.''04$) 7-mm continuum observations of L1551

Table 2. Observed CS ($J = 7-6$) and HCN ($J = 4-3$) line parameters toward the protostellar positions

Source	CS ($J = 7-6$)					HCN ($J = 4-3$)				
	$\int T_{MB} dv^*$ (K km s $^{-1}$)	T_{MB}^* (K)	rms (K)	Δv^* (km s $^{-1}$)	v_{LSR}^* (km s $^{-1}$)	$\int T_{MB} dv^*$ (K km s $^{-1}$)	T_{MB}^* (K)	rms (K)	Δv^* (km s $^{-1}$)	v_{LSR}^* (km s $^{-1}$)
L1551 IRS 5	2.12 [†]	1.61 [†]	0.10	0.92 [†]	6.45 [†]	1.70 [†]	1.32 [†]	0.12	0.88 [†]	6.29 [†]
L1551 NE	1.26	0.46	0.19	2.57	7.18	-	-	0.20	-	-
IRAS 16293-2422	31.05 [†]	9.12 [†]	0.12	2.68 [†]	3.56 [†]	19.41 [‡]	5.79 [‡]	0.08	- [‡]	3.48 [‡]
L43	0.68 [§]	0.52 [§]	0.18	0.44 [§]	0.11 [§]	0.85	1.06	0.19	0.75	0.41
L483	2.61	1.80	0.22	1.36	5.52	1.87	0.84	0.21	2.09	5.62
L723	1.21	0.74	0.12	1.54	11.24	1.18	0.36	0.09	3.07	11.09
B335	1.91	1.20	0.15	1.49	8.18	0.43	0.58	0.14	0.69	8.06

*Derived from the one-component Gaussian fitting to the spectra unless otherwise noted. Here, T_{MB} , Δv , and v_{LSR} are the peak main-beam brightness temperature, FWHM width, and the central LSR velocity of the Gaussian, respectively. $\int T_{MB} dv$ is the integrated value of the Gaussian.

[†]Non-Gaussian spectral shapes. T_{MB} , Δv , v_{LSR} , and $\int T_{MB} dv$ are the peak main-beam brightness temperature, FWHM line width, velocity of the emission peak, and the integrated intensity over the velocity range from $v_{LSR} = 4.0$ to 9.0 km s $^{-1}$ for L1551 IRS 5 and -7.0 to 13.0 km s $^{-1}$ for IRAS 16293-2422, respectively.

[‡]Self-absorbed spectral shape. T_{MB} , v_{LSR} , and $\int T_{MB} dv$ are the peak main-beam brightness temperature, velocity of the emission peak, and the integrated intensity over the velocity range from $v_{LSR} = -7.0$ to 13.0 km s $^{-1}$, respectively.

[§]Marginal detection and the line parameters are less reliable. T_{MB} , Δv , v_{LSR} , and $\int T_{MB} dv$ are the peak main-beam brightness temperature, FWHM line width, velocity of the emission peak, and the integrated intensity over the velocity range from $v_{LSR} = -2.0$ to 1.5 km s $^{-1}$, respectively.

IRS 5 with VLA have found that L1551 IRS 5 is a triple protostellar system with a projected separation of ~ 47 AU and ~ 13 AU (Lim & Takakuwa 2006). SMA observations of L1551 IRS 5 in the CO (2–1) line within the ~ 4000 AU region have found multiple molecular outflows, one of which shows precessing motion presumably due to the tidal interaction of the circumstellar disks around the multiple protostars (Wu, Takakuwa, & Lim 2009). Interferometric observations of L1551 IRS 5 in millimeter molecular lines of CS (2–1), H 13 CO $^+$ (1–0), and C 18 O (1–0) have revealed a ~ 2000 - 5000 AU-scale molecular envelope surrounding L1551 IRS 5, which is elongated perpendicularly to the outflow axis (Ohashi et al. 1996; Saito et al. 1996; Momose et al. 1998). Along the outflow direction the south-western and north-eastern parts of the envelope are blueshifted and redshifted, whereas across the outflow direction the north-western and south-eastern parts are redshifted and blueshifted, respectively. The velocity gradients seen in the envelope along and across the outflow direction have been interpreted as an infalling and rotating gas motion in the envelope, respectively (Ohashi et al. 1996; Saito et al. 1996; Momose et al. 1998). On the other hand, SMA observations of L1551 IRS 5 in the submillimeter CS (7–6) line have found a compact (~ 500 AU) molecular gas with mainly rotating motion around the protostar (Takakuwa et al. 2004). With the present ASTE observations of L1551 IRS 5 we can investigate the extent and kinematics of the warm gas traced in the submillimeter molecular lines and the relation with the infalling envelope traced in the millimeter lines.

Figure 3 shows total integrated intensity maps of the CS ($J = 7-6$) (*left panel*) and HCN ($J = 4-3$) (*right*) lines in L1551 IRS 5. Figures 4 and 5 show relevant line profile maps of the CS ($7-6$) and HCN ($4-3$) lines, respectively. There are intense blobs centered on the protostellar position both in the CS and HCN emissions. Both the CS and HCN emission distributions show a slight elongation toward the south-west of the protostar. The shapes of the emission distributions do not resemble the shape of the ASTE beam, suggesting that the submillimeter emissions are slightly resolved. Two-dimensional Gaussian fittings to the submillimeter emission distributions show that the deconvolved size of the HCN emission is $\sim 18'' \times 15''$ ($= 2600 \text{ AU} \times 2100 \text{ AU}$; $\text{PA} = 65^\circ \pm 12^\circ$), and that in the CS emission only the major axis ($\text{PA} = 70^\circ \pm 1^\circ$) is resolved ($\sim 18''$). The deconvolved sizes are smaller than the ASTE beam size and hence the estimated emission extents are not well-determined. In order to unambiguously measure the extent of the submillimeter molecular emission, we combined the present ASTE CS ($7-6$) data with our published SMA CS ($7-6$) data (Takakuwa et al. 2004). The *middle* and *right* panels in Figure 6 show the combined ASTE + SMA total integrated intensity maps of the CS ($7-6$) emission in L1551 IRS 5 before and after the primary beam correction, respectively. The submillimeter CS emission in L1551 IRS 5 consists of two components; one is a compact ($\lesssim 500 \text{ AU}$) component centered on the protostellar positions, and the other a halo-like, extended ($\sim 2000 \text{ AU}$) component, delineated by brown dashed curves in Figure 6. The central compact CS ($7-6$) component is also seen in the SMA-only image, which shows rotating gas motion inside the infalling envelope seen in the C^{18}O ($1-0$) line (Takakuwa et al. 2004). The combined image shows another submillimeter CS component, which appears to extend toward the associated reflection nebula and hence the direction of the blueshifted molecular outflow, and the extension of this submillimeter emission component appears to be perpendicular to that of the C^{18}O ($1-0$) envelope (see Figure 6 *left*). The “asymmetric”, elongated distribution of the submillimeter molecular emissions toward the direction of the blueshifted molecular outflow is also seen in L483 (Paper I).

The CS ($7-6$) line profile map shows that the emission peaks at the southwest of the protostar tend to be redshifted and at the northeast blueshifted (Figure 4, see spectra with blue and red rectangles), although in the HCN ($4-3$) line profile map such a velocity structure is not clear (Figure 5). This velocity feature in the submillimeter CS line appears to be opposite to that of the infalling envelope seen in the millimeter C^{18}O and H^{13}CO^+ ($1-0$) lines (Saito et al. 1996; Momose et al. 1998), and that of the CO outflows (Stojimirović et al. 2006; Moriarty-Schieven et al. 2006; Wu, Takakuwa, & Lim 2009). Opposite velocity gradients of the submillimeter molecular lines from those of the millimeter lines and the associated outflows are also seen in L483 and B335 (Paper I). In §4.2., we will present quantitative analyses of the submillimeter velocity gradients in these protostellar sources and discuss their origin.

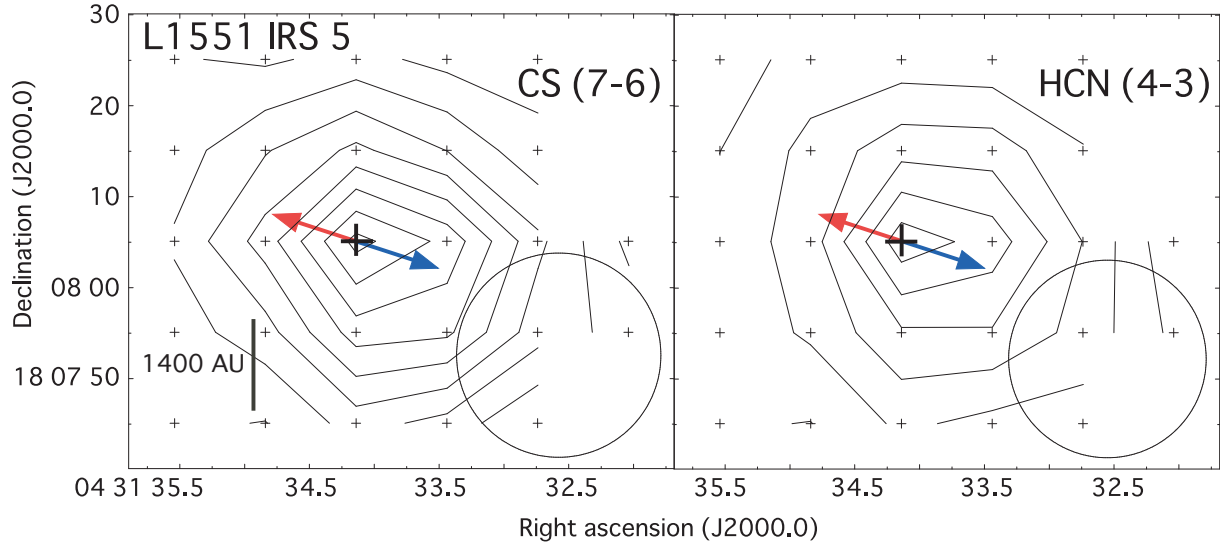


Fig. 3. Total integrated intensity maps of the CS (7–6) (*left*) and HCN (4–3) (*right*) emission in L1551 IRS 5 over the velocity range of 5.3 - 8.0 km s⁻¹ observed with ASTE. Contour levels are from 2 σ in steps of 4 σ (1 σ = 0.0605 K km s⁻¹). The highest contours in the CS and HCN maps are 30 σ and 22 σ , respectively. Crosses indicate observed positions. Red and blue arrows show the direction of the redshifted and blueshifted molecular outflow, respectively, and the roots of the arrows with large crosses indicate the protostellar position. An open circle at the bottom-right corner in each panel shows the ASTE beam.

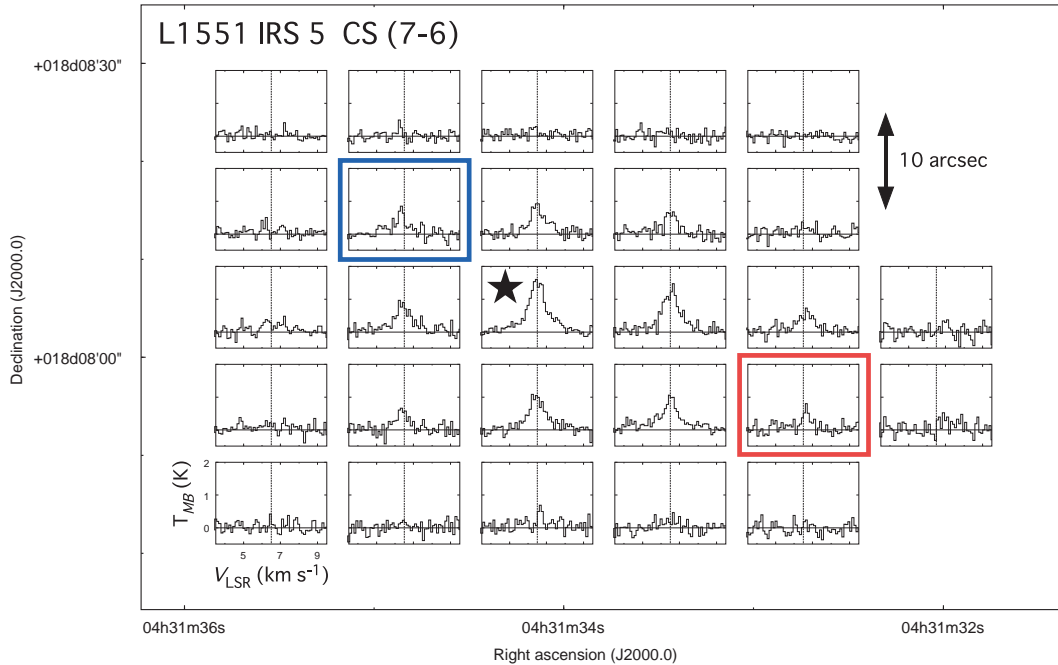


Fig. 4. Stamp map of the CS (7–6) line profile in L1551 IRS 5 observed with ASTE. The line profile with a star mark is the profile toward the central stellar position. Solid horizontal lines show zero levels, and dashed vertical lines systemic velocity of 6.5 km s⁻¹.

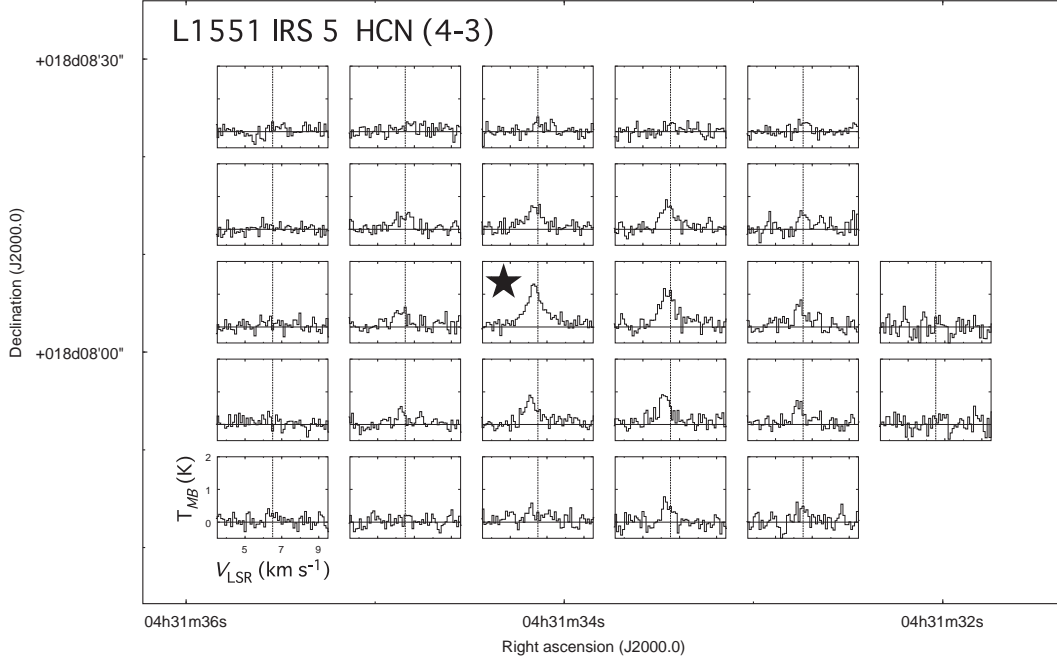


Fig. 5. Same as Figure 4 but for the HCN (4–3) line profile.

3.2.2. L1551 NE

L1551 NE is the second brightest ($\sim 4.2 L_{\odot}$) protostellar source in Taurus, located $\sim 2'5$ north-east of L1551 IRS 5 (Emerson et al. 1984). L1551 NE is classified as a Class I protostar based on its spectral energy distribution (Froebrich 2005). Radio continuum observations by Rodríguez et al. (1995) and Reipurth et al. (2002) have revealed two compact sources with a separation of ~ 70 AU and a position angle of $\sim 300^{\circ}$, suggesting that L1551 NE is a protostellar binary. Optical and NIR observations of L1551 NE have found Herbig-Haro objects HH 28, HH 29, HH 454, and a collimated [Fe II] jet, and a bright reflection nebula (Draper et al. 1985; Hodapp & Ladd 1995; Devine et al. 1999; Reipurth et al. 2000; Hayashi & Pyo 2009). With JCMT, Moriarty-Schieven et al. (1995a) detected blueshifted ($\sim 3 - 5$ km s $^{-1}$ from the systemic velocity) emission in the wing of the CO (3–2) line toward L1551 NE that coincides spatially with its optical/infrared reflection nebula, suggesting that the blueshifted emission traces the molecular outflow driven by L1551 NE. Millimeter interferometric observations of L1551 NE in the CS (2–1, 3–2) lines revealed a compact (~ 700 AU) dense-gas component associated with the central protostar plus a NW-SE elongated (~ 6000 AU) component located toward ~ 1000 AU west from the protostar (Yokogawa et al. 2003). On the other hand, interferometric observations of the H 13 CO $^{+}$ (1–0) line show a NW-SE elongated (~ 8000 AU) component located toward ~ 700 AU east of the protostar (Saito et al. 2001). The prominent redshifted molecular outflow from L1551 IRS5 passes in projection through the location of L1551 NE, and likely impacts the molecular envelope around L1551 NE. The anti-correlation between the CS and H 13 CO $^{+}$ emissions may be due to the shock chemistry (Plambeck & Snell

L1551 IRS 5

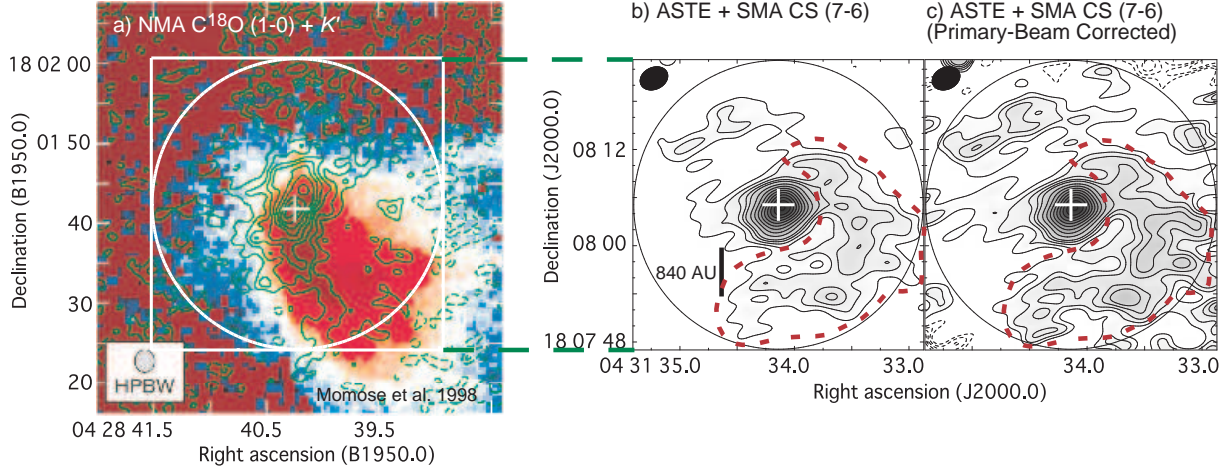


Fig. 6. a) Total integrated intensity map of the C^{18}O (1–0) emission observed with NMA (green contours) superposed on the K' -band image of the associated reflection nebula in L1551 IRS 5, taken from Fig. 2 by Momose et al. (1998). Contour levels start from 1.5σ in steps of 1.5σ ($1 \sigma = 0.679 \text{ K}$). A white cross indicates the protostellar position, and a filled ellipse at the bottom-left corner shows the NMA beam ($2''.8 \times 2''.5$, P.A. = 0°). An open circle and square show the SMA Field of View and the imaging region of the SMA images shown in middle and right panels. b) Combined ASTE + SMA image of the CS (7–6) emission in L1551 IRS 5. Contour levels are from 2σ in steps of 1σ ($1 \sigma = 0.904 \text{ K km s}^{-1}$). The integrated velocity range is from 5.4 km s^{-1} to 8.4 km s^{-1} . A cross and an open circle indicate the protostellar position and the SMA Field of View, respectively. A filled ellipse at the top-left corner shows the synthesized beam ($3''.6 \times 2''.7$, P.A. = -65°). A brown dashed contour delineates the extended, halo-like CS component (see text). c) Combined ASTE + SMA image of the CS (7–6) emission in L1551 IRS 5 after the primary beam correction. Contour levels and symbols are the same as those in the middle panel.

1995; Yokogawa et al. 2003).

Figures 7 and 8 show line profile maps of the CS (7–6) and HCN (4–3) emissions in L1551 NE, respectively. Figure 9 shows the relevant total integrated intensity maps of the CS (7–6) (*left panel*) and HCN (4–3) (*right*) lines in L1551 NE (red contours), superposed on the $[\text{Fe II}] + 1.64\text{-}\mu\text{m}$ continuum image taken with SUBARU (Hayashi & Pyo 2009). Although the submillimeter molecular emissions are not spatially resolved with the ASTE $22''$ beam, their peak positions appear to be $\sim 10''$ west from the protostellar position. Along the east-west direction passing through the central protostellar position, the CS integrated intensity from $-20''$ to $+10''$ of the protostar exceeds above the 8σ level, and the HCN integrated intensity from $-10''$ to $+10''$ above 4σ level. Taking into account the detection levels, the ASTE pointing error ($\sim 2''$) and the beam size, we consider that these $\sim 10''$ offsets of the submillimeter emission peaks from the protostellar position are real. These offsets of the emission distributions resemble those of the millimeter CS (2–1, 3–2) emission distributions (Yokogawa et al. 2003). We also note that the offsets of the submillimeter molecular emissions are toward the direction of the

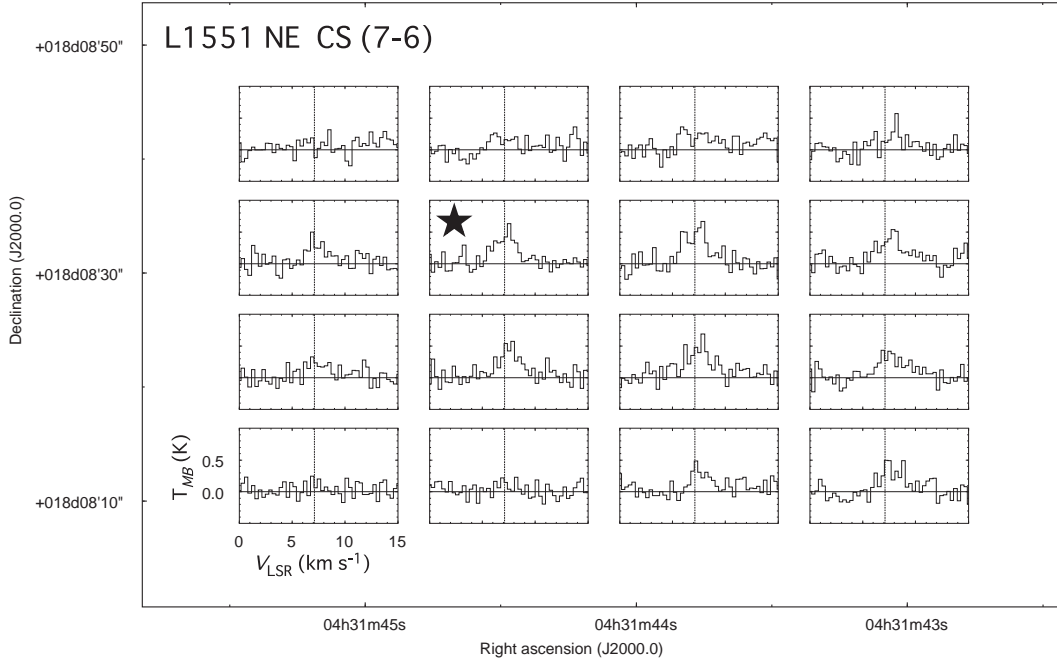


Fig. 7. Stamp map of the CS (7–6) line profile in L1551 NE observed with ASTE. The line profile with a star mark is the profile toward the central stellar position. Solid horizontal lines show zero levels, and dashed vertical lines systemic velocity of 7.1 km s^{-1} . Three-channel bindings were performed to increase the signal-to-noise ratio of the spectra.

associated reflection nebula seen in the SUBARU image, which is similar to the case of L1551 IRS 5 (Fig. 6).

3.2.3. L723 and L43

L723 is another Class 0 candidate with a luminosity of $\sim 3.3 L_{\odot}$ at a distance of 300 pc (Davidson 1987). In L723 there are at least four centimeter sources; VLA 1, and VLA 2A, 2B, and 2C, and one 7-mm source; VLA 2D (Anglada et al. 1991; Carrasco-González et al. 2008). VLA 1 is located at ~ 4500 AU south-west from the VLA 2 complex, and only the VLA2 complex is associated with dense molecular gas seen in the millimeter CS (1–0, 2–1, 3–2) lines as well as the X-shaped CO outflow (Hayashi et al. 1991; Hirano et al. 1998). The peaks of the CS (2–1, 3–2) emission distributions are offset by $\sim 10''$ east from the VLA 2 complex (Hirano et al. 1998). SMA observations of L723 have found two compact (~ 600 AU) dusty cores at a projected separation of ~ 880 AU (SMA 1 and SMA 2), where SMA 1 is associated with VLA 2D and SMA 2 VLA 2A, 2B, and 2C (Girart et al. 2009). Both SMA 1 and 2 show marginal evidence of infalling and rotating gas motion in the H_2CO ($3_{0,3}-2_{0,2}$) line, whereas only SMA 2 appears to be associated with HH objects and multiple (at least three) molecular outflows driven by the three different protostellar sources (Carrasco-González et al. 2008; Girart et al. 2009).

Figures 10, 11, and 12 show line profile maps of the CS (7–6) and HCN (4–3) emission,

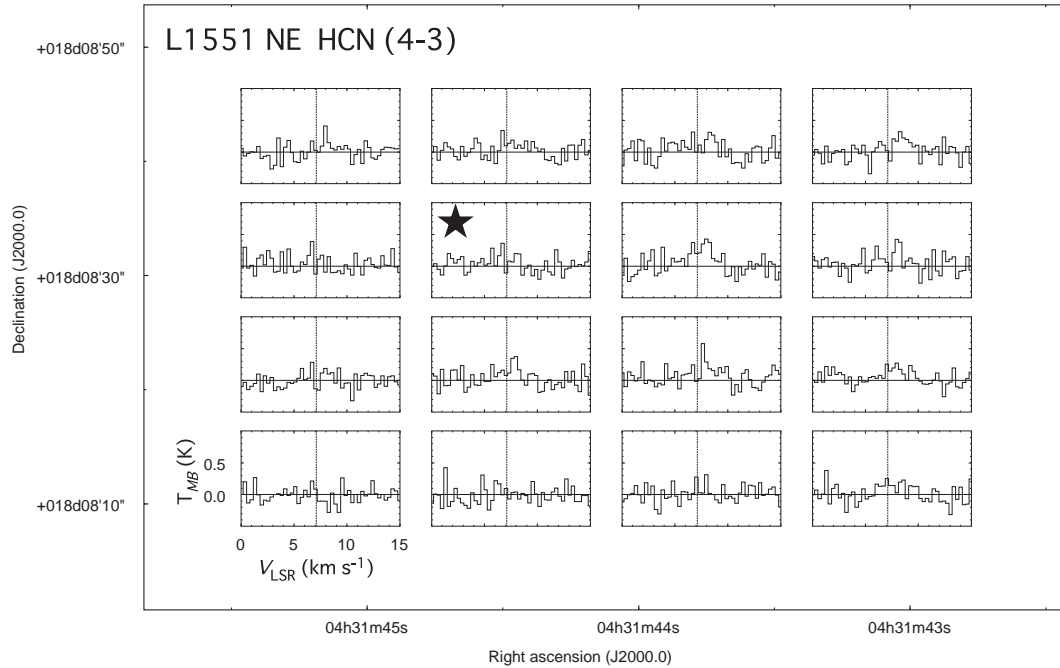


Fig. 8. Same as Figure 7 but for the HCN (4-3) emission.

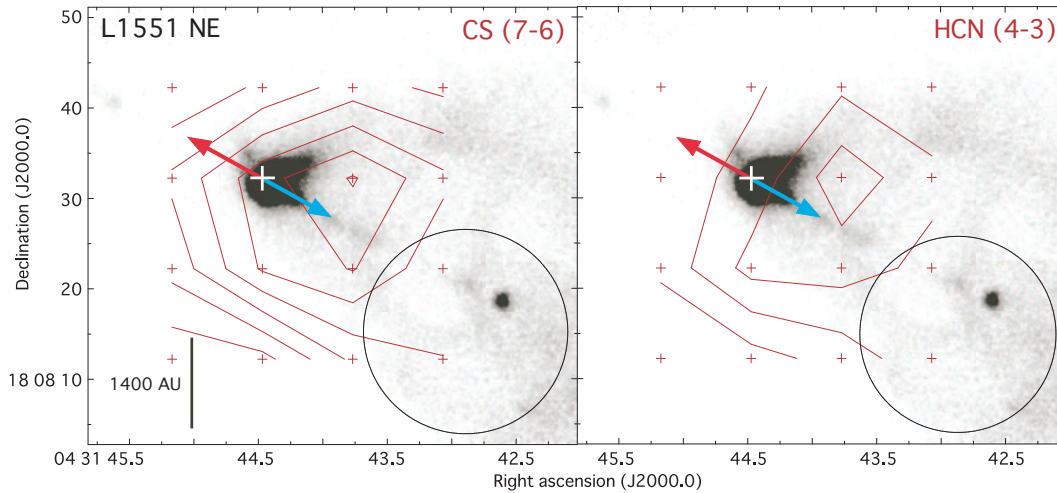


Fig. 9. Total integrated intensity maps of the CS (7-6) (*left*) and HCN (4-3) (*right*) emission in L1551 NE over the velocity range of 5.6 - 8.7 km s⁻¹ observed with ASTE, superposed on the [Fe II] + 1.64- μ m continuum image taken with SUBARU in grey scale (Hayashi & Pyo 2009; The large black blob associated with the protostar is the reflection nebula, and the small blob at the south-west of the protostar is HH 454A.). Contour levels are from 2 σ in steps of 2 σ (1 σ = 0.080 K km s⁻¹). The highest contours in the CS and HCN maps are 16 σ and 8 σ , respectively. Crosses indicate observed positions. Red and blue arrows show the direction of the redshifted and blueshifted molecular outflow, respectively, and the roots of the arrows with white crosses indicate the protostellar position. An open circle at the bottom-right corner in each panel shows the ASTE beam.

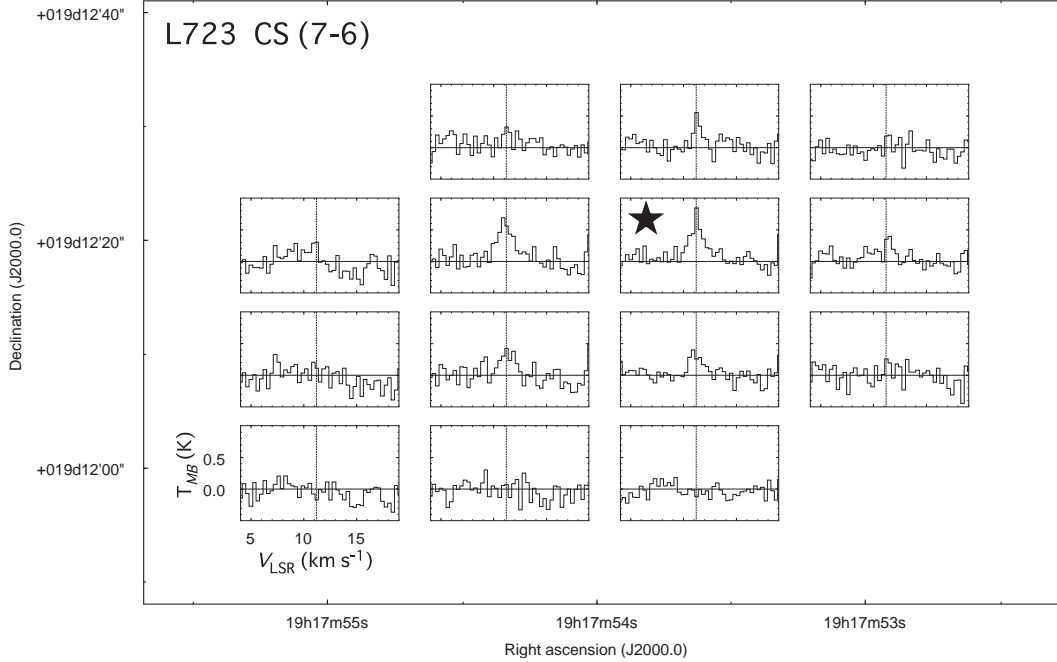


Fig. 10. Stamp map of the CS (7–6) line profile in L723 observed with ASTE. The line profile with a star mark is the profile toward the central stellar position. Solid horizontal lines show zero levels, and dashed vertical lines systemic velocity of 11.2 km s^{-1} . Three-channel bindings were performed to increase the signal-to-noise ratio of the spectra.

and the corresponding total integrated intensity maps in L723, respectively. The CS and HCN total integrated intensities toward VLA 2 exceed $> 13\sigma$, whereas those toward VLA 1 are below 3σ . These results suggest that only VLA 2 is associated with the dense and/or warm molecular gas traced by the submillimeter molecular lines, which is consistent with the previous millimeter observations (Hirano et al. 1998; Girart et al. 2009). The intensity of the CS emission at $10''$ east of the protostar is comparable to that at the protostellar position ($\sim 14 \sigma$), and is much higher than that at $10''$ west ($\sim 6 \sigma$). The HCN intensity at $10''$ east ($\sim 10 \sigma$) is also higher than that at $10''$ west ($\sim 6 \sigma$). Although the ASTE observations do not resolve the submillimeter emissions in L723, the differences of the submillimeter intensities between $10''$ east and west of the protostar are probably real. Hence, the peaks of the submillimeter emission distributions in L723 are likely offset from the protostellar position, as in the case of L1551 NE. The millimeter CS (2–1, 3–2) emission distributions also show similar peak offsets by $\sim 10''$ east from the protostar (Hirano et al. 1998). The direction of these offsets is toward the associated blueshifted outflow.

Figures 13 and 14 show line profile maps of the CS (7–6) and HCN (4–3) emission in L43, respectively. L43 (*or* RNO 91, IRAS 16316-1540) is a Class I - II protostar with $L_{bol} \sim 2.7 L_{\odot}$ and $T_{bol} \sim 370 \text{ K}$ (Shirley et al. 2000; Anglada & Rodríguez 2002; Chen et al. 2009), and hence somewhat a more evolved source than the other sources of our sample. The protostar is

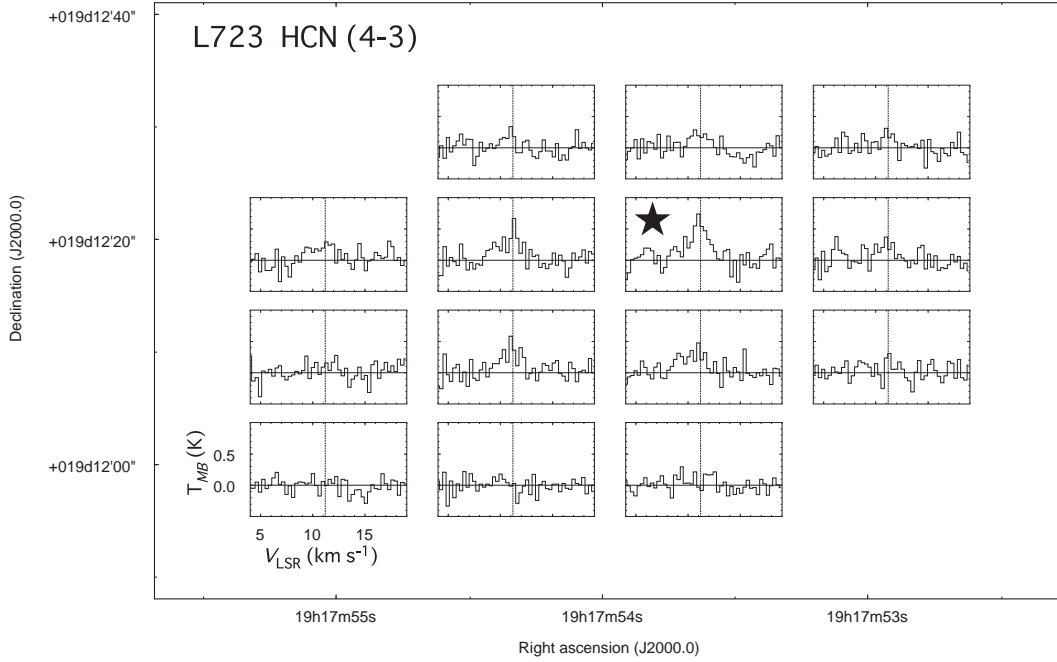


Fig. 11. Same as Figure 10 but for the HCN (4-3) emission.

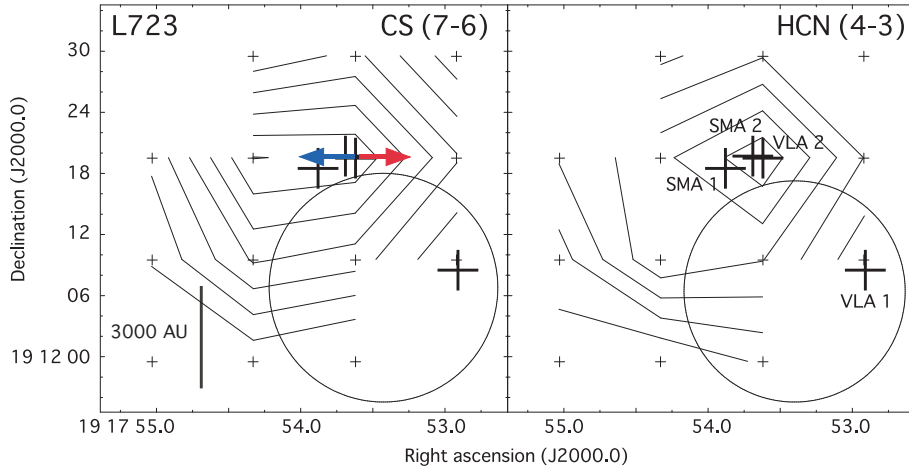


Fig. 12. Total integrated intensity maps of the CS (7-6) (*left*) and HCN (4-3) (*right*) emission in L723 over the velocity range of 9.9 - 12.1 km s⁻¹ observed with ASTE. Contour levels are from 2 σ in steps of 2 σ (1 σ = 0.072 K km s⁻¹). The highest contours in the CS and HCN maps are 14 σ and 12 σ , respectively. Small crosses indicate observed positions, and large crosses positions of VLA 1, VLA 2 (A, B, C), SMA 1, and SMA 2, as labeled in the figure. Red and blue arrows show the direction of the redshifted and blueshifted molecular outflow driven from VLA 2, respectively. An open circle at the bottom-right corner in each panel shows the ASTE beam.

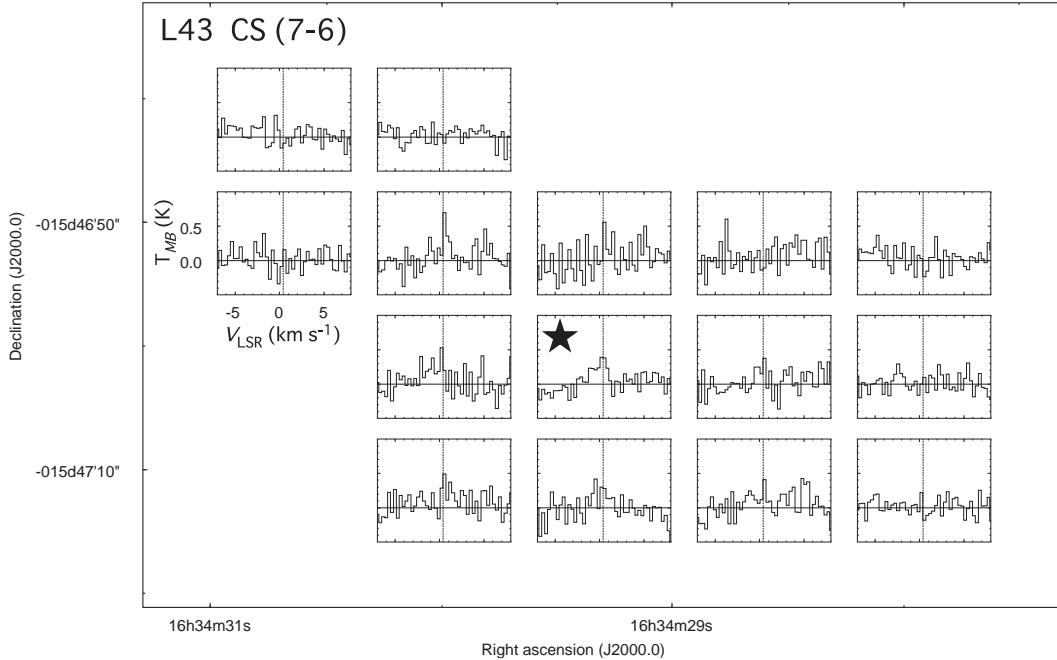


Fig. 13. Stamp map of the CS (7–6) line profile in L43 observed with ASTE. The line profile with a star mark is the profile toward the central stellar position. Solid horizontal lines show zero levels, and dashed vertical lines systemic velocity of 0.4 km s^{-1} . Three-channel bindings were performed to increase the signal-to-noise ratio of the spectra.

associated with an ~ 4000 -AU scale dusty envelope (Shirley et al. 2000; Chen et al. 2009), and a bipolar molecular outflow along the SE - NW direction (Bence et al. 1998; Lee et al. 2000; Lee et al. 2002). Figures 13 and 14 show that the signal-to-noise ratio of the submillimeter molecular lines is not high enough to discuss their spatial distributions. One interesting point is that L43 is the only source in our ASTE observations with the HCN (4–3) emission more intense than the CS (7–6) emission. This could be related to the later protostellar evolutionary stage of L43 than that of the other sources.

4. Discussion

4.1. “Skewed” Distributions of the Submillimeter Molecular Emissions

As described in the previous section, the submillimeter CS (7–6) and HCN (4–3) emissions toward low-mass protostars often show “skewed” distributions with respect to the protostellar positions. The combined ASTE + SMA image of the CS emission in L1551 IRS 5 illustrates that there is a halo-like component elongated (~ 2000 AU) toward the associated reflection nebula and the blueshifted outflow, as well as a central compact ($\lesssim 500$ AU) component centered on the protostellar position. In L1551 NE, the emission peaks of the CS and HCN lines are likely offset from the protostellar position, and are shifted toward the associated reflection nebula. Similar peak offsets of the submillimeter CS and HCN emissions are also seen in L723.

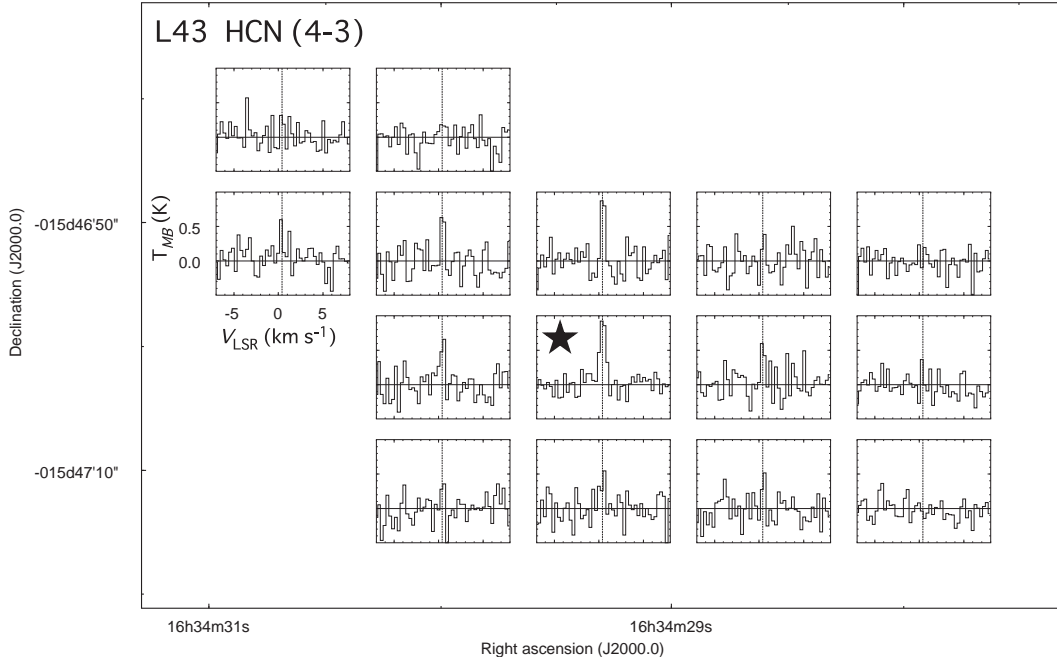


Fig. 14. Same as Figure 13 but for the HCN (4-3) emission.

In L483, we found possible extensions of the CS (~ 2300 AU) and HCN (~ 5500 AU) emissions toward the direction of the associated reflection nebula and the blueshifted outflow (Paper I). The combined ASTE + SMA CS (7–6) image in B335, another Class 0 protostar, also shows an elongated (~ 2000 AU) component tracing the reflection nebula as well as a compact ($\lesssim 500$ AU) component centered on the protostellar position (Yen, Takakuwa, & Ohashi 2011). These results indicate that the asymmetric, or “skewed” distributions of the submillimeter molecular emissions toward the associated reflection nebulae are relatively frequent.

One possible interpretation of these results is that the extended submillimeter molecular emissions at a few thousands AU scale trace “walls” of the cavity of the envelope evacuated by the associated outflows. In Figure 15 we show a schematic diagram to explain the skewed distribution of the submillimeter molecular emissions. At the surface of the cavity wall molecular gas is irradiated by the stellar photons and hence the gas temperature is likely to be higher than that at the midplane (Nakazato et al. 2003; Whitney et al. 2003). As discussed in Paper I, the submillimeter CS and HCN emissions likely trace warmer ($\gtrsim 40$ K) molecular gas than that traced by millimeter molecular emissions, and hence the warmer cavity walls are selectively traced by the submillimeter molecular emissions whereas the colder, midplane regions are traced by the millimeter emissions. Here, at the side of the associated reflection nebula the wall is directly seen along the line of sight, while at the other side the wall is likely obscured by the cold foreground envelope gas. The skewness of the submillimeter molecular emissions, where the submillimeter emissions are bright only at the side of the associated reflection nebula, may be explained by the foreground absorption along the line of sight.

In order to illustrate this possibility, we performed simple calculations based on the Large Velocity Gradient (LVG) model (Goldreich & Kwan 1974; Scoville & Solomon 1974). The brightness temperature of the submillimeter emission at the obscured side ($\equiv T_{obs}$) can be written as,

$$T_{obs} = T_{re}e^{-\tau} + J(T_{ex})(1 - e^{-\tau}) - J(T_{bg}), \quad (2)$$

where

$$J(T) = \frac{\frac{h\nu}{k}}{\exp(\frac{h\nu}{kT}) - 1}. \quad (3)$$

In the above expressions, h is the Planck constant, k is Boltzmann's constant, ν is the line frequency, T_{ex} and τ are the excitation temperature and the optical depth in the foreground cloud, T_{bg} is the microwave background radiation temperature ($= 2.725$ K), and T_{re} is the brightness temperature of the submillimeter emission from the warm cavity wall at the rear side, respectively. For simplicity, T_{re} is fixed to be the peak brightness temperature of the halo-like CS emission in L1551 IRS 5 ($\equiv 9.2$ K; see Fig. 6). We calculated T_{ex} and τ in the foreground cloud with a gas kinetic temperature of 10 K for a different gas density ($\equiv n_{H_2}$) and CS abundance per unit velocity gradient ($\equiv X(CS)/dV/dR$) based on the LVG model, and then derived T_{obs} as a function of the foreground gas density and the abundance. Details of our LVG calculation are described in Paper I. In Figure 16 we show calculated T_{obs} and τ as a function of n_{H_2} for different $X(CS)/dV/dR$. A horizontal dashed line in the upper panel shows the 3σ upper limit of the combined ASTE + SMA CS (7–6) data (~ 3.6 K). This figure illustrates that if the foreground cloud is optically thick against the submillimeter CS emission, the emission from the rear side could be significantly absorbed, down to the sensitivity limit of the ASTE + SMA CS (7–6) data. The range of the foreground gas density where the line intensity along the line of sight is lower than the sensitivity limit depends on adopted $X(CS)/dV/dR$. The typical $X(C^{34}S)/dV/dR$ value in cold dark clouds was estimated to be $\sim 5.0 \times 10^{-11}$ km $^{-1}$ s pc from the multi-transitional C 34 S (1–0, 2–1) observations (Takakuwa et al. 2000). Then the typical $X(CS)/X(C^{34}S)$ ratio of 22 (Chin et al. 1996) yields $X(CS)/dV/dR = X(C^{34}S)/dV/dR \times 22 \sim 10^{-9}$. With $X(CS)/dV/dR = 10^{-9}$ the density range is $\sim 10^{5.5-6.3}$ cm $^{-3}$, which is typical in cloud cores, and the optical depth ranges from ~ 1 to ~ 14 .

Two-dimensional radiative transfer models of protostellar envelopes (Spaans et al. 1995; Nakazato et al. 2003; Whitney et al. 2003) are likely to support our interpretation that the extended submillimeter molecular emissions at a few thousands AU scale trace walls of the cavity of the envelopes evacuated by the associated outflows. Spaans et al. (1995) suggested that the narrow ^{12}CO and ^{13}CO $J=6-5$ emissions detected toward many low-mass young stellar objects are produced at the wall of the cavity evacuated by the bipolar outflow, heated by the radiation field generated in the inner part of the accretion disk. Nakazato et al. (2003) and Whitney et al. (2003) demonstrated that at the surface of the wall of the cavity

opened by the outflow in the envelope the gas temperature becomes higher than that predicted from spherically symmetric models, due to the heating by the protostellar photons. In fact, the intensities of the submillimeter molecular lines observed with the ASTE 22'' beam appear to correlate with the central protostellar luminosities, as discussed in §3.1. To quantitatively show this trend, we compiled published CS (7–6) data (Blake et al. 1995; Moriarty-Schieven et al. 1995b) and protostellar luminosities (Moriarty-Schieven et al. 1994; Froebrich 2005). In Figure 17 we plot integrated intensities of the CS (7–6) emission versus bolometric luminosities of the protostellar sources. The data points with filled circles are from Tables 1 and 2 in the present paper. There is a clear linear correlation between the source bolometric luminosities and the submillimeter CS intensities, and the least square fitting to the data points yields $I_{CS} \propto L_{bol}^{0.92}$. The linear correlation between the source luminosities and the intensities of the submillimeter molecular emission may also support the idea that the submillimeter molecular emission at a few thousands AU scale traces the wall of the envelope cavities heated by the protostars. Detailed physical and chemical models of the envelopes and the 3-dimensional radiative transfer calculations should help to understand the distributions and the origins of the submillimeter molecular lines in protostellar envelopes.

4.2. *Different Kinematics between the Millimeter and Submillimeter Molecular Lines in the Protostellar Envelopes*

In Paper I, we suggested that in L483 and B335 the submillimeter molecular lines show opposite velocity gradients to those of the millimeter lines and the outflows along the outflow axis. As mentioned in §3.2.1, from our new ASTE data we found that the submillimeter CS emission in L1551 IRS 5 is also likely to show a similar, opposite velocity gradient. In this final subsection, we will show how significant these opposite velocity gradients in the submillimeter molecular line are with our statistical analyses, and discuss the origin of the opposite velocity gradients.

To unambiguously assess the statistical significance of the velocity gradients, we adopted a method described by Goodman et al. (1993). We first fit a single Gaussian function to each spectrum whose peak intensity is above 3σ , to derive the central *LSR* velocity of each spectrum ($\equiv v_{LSR}$). The error of the derived central velocity ($\equiv \sigma_{v_{LSR}}$) can be estimated as

$$\sigma_{v_{LSR}} = 1.15 \left(\frac{\sigma_T}{T} \right) (\delta_v \Delta v)^{\frac{1}{2}}, \quad (4)$$

where T is the peak of a Gaussian fit to the line profile, Δv is the FWHM line width of a Gaussian fit, σ_T is the rms noise in the spectrum, and δ_v is the ASTE velocity resolution (Landman et al. 1982). Then, we fit a plane function to the estimated central velocities with the errors at the different positions as,

$$v_{LSR} = v_0 + a\Delta\alpha + b\Delta\delta, \quad (5)$$

where $(\Delta\alpha, \Delta\delta)$ denotes the positions of the spectra with respect to the central protostellar

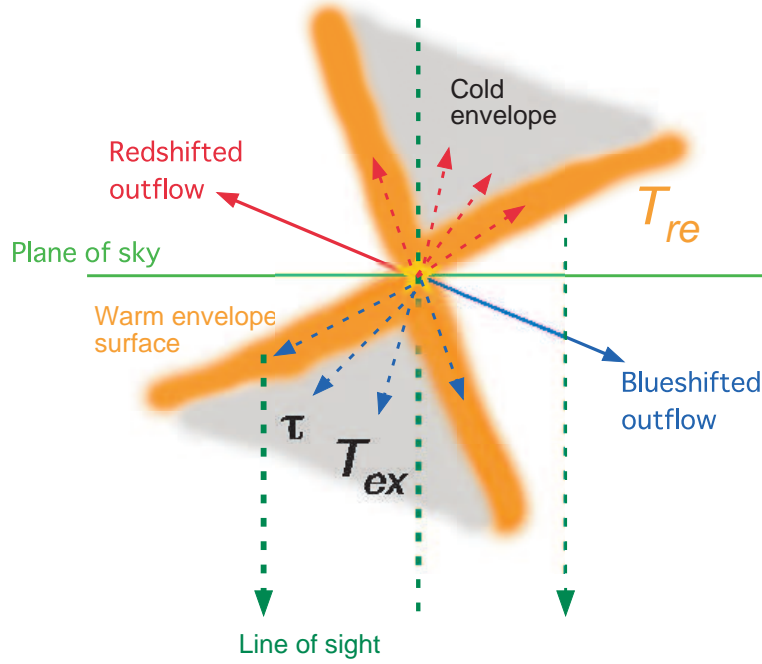


Fig. 15. Schematic diagram of the envelope configuration to explain the observed skewed distribution and the velocity gradient of the submillimeter molecular emissions. The orange area denotes the region of the warm surface of the cavity wall in the envelope, where the submillimeter molecular emissions arise. The gray area indicates the cold inner envelope. The star mark shows the central protostar, and the blue and red arrows the associated blueshifted and redshifted outflows, respectively. The horizontal green line shows the plane of the sky, whereas the vertical dashed arrows the line of sight. T_{re} , T_{ex} , and τ denote the brightness temperature of the submillimeter molecular emission at the cavity wall, the excitation temperature and the optical depth of the submillimeter emission in the cold inner envelope, respectively. In reality, the cavity wall is also present at the foreground and the background of the paper, and the dashed arrows denote the dispersing gas motion at the cavity wall. This figure illustrates that at the side of the blueshifted outflow the submillimeter molecular emission from the warm cavity surface is seen directly whereas at the side of the redshifted outflow the emission is absorbed by the cold foreground envelope component. Furthermore, at the side of the blueshifted outflow the envelope dispersing motion is mostly observed as a redshifted submillimeter emission whereas at the side of the redshifted outflow as a blueshifted submillimeter emission.

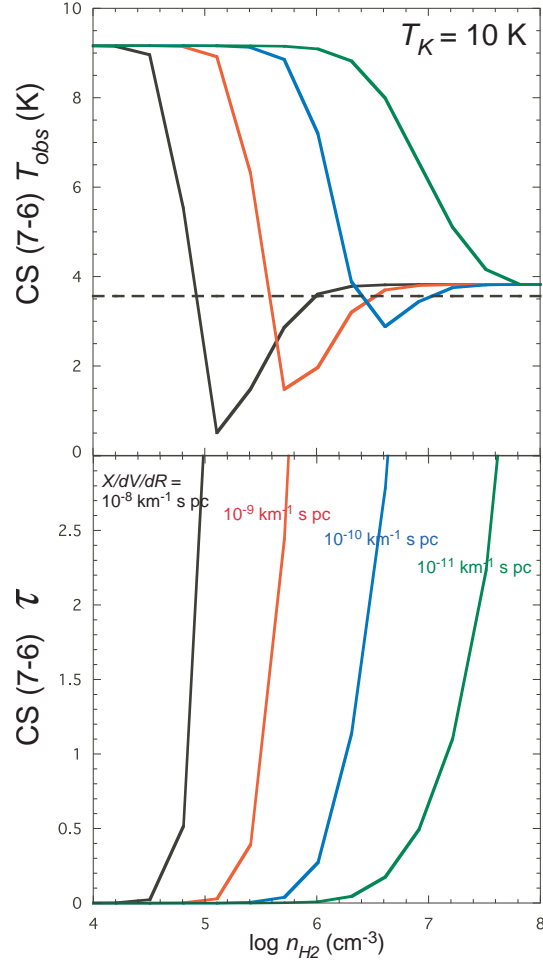


Fig. 16. Result of our statistical equilibrium calculations of the CS (7–6) emission. The background CS (7–6) intensity is fixed to be 9.2 K, the observed peak intensity at the south-western extended CS (7–6) emission component in L1551 IRS 5. We calculated the excitation temperature and the optical depth of the CS (7–6) emission in the foreground cloud component with the LVG model, and then calculated the CS intensity along the line of sight. Upper and lower panels show the calculated CS (7–6) brightness temperature and the optical depth, respectively, as a function of the molecular-gas density in the foreground cloud with a kinetic temperature of 10 K, and $X/dV/dR$ values of $10^{-8} \text{ km}^{-1} \text{ s pc}$ (black curve), $10^{-9} \text{ km}^{-1} \text{ s pc}$ (red), $10^{-10} \text{ km}^{-1} \text{ s pc}$ (blue), and $10^{-11} \text{ km}^{-1} \text{ s pc}$ (green). A horizontal dashed line in the upper panel shows the 3σ upper limit of the combined ASTE + SMA CS (7–6) data. This figure illustrates that under the presence of cold dense foreground molecular gas the CS (7–6) emission can be significantly absorbed.

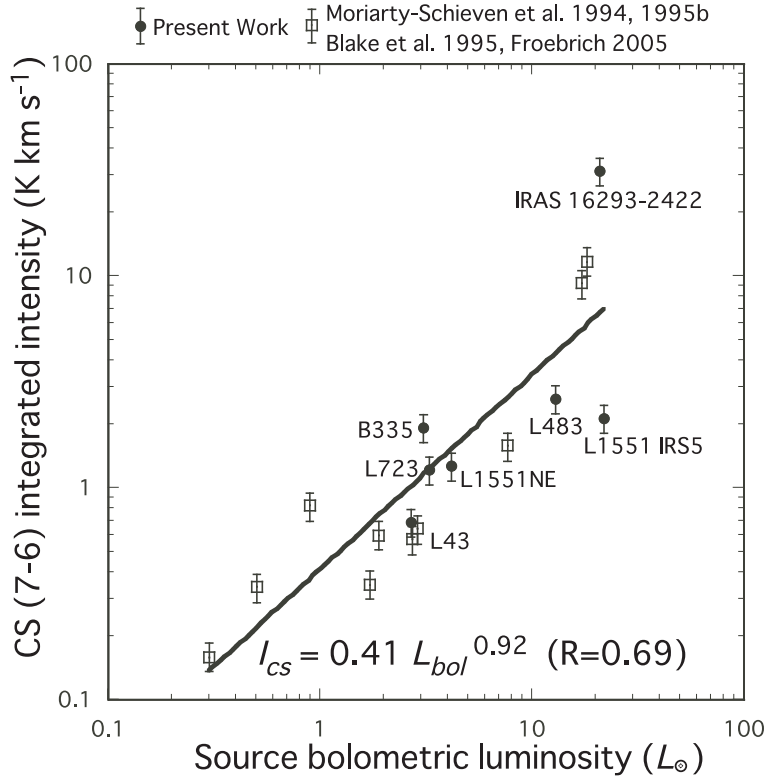


Fig. 17. Correlation diagram between bolometric luminosities of the protostellar sources and integrated intensities of the submillimeter CS (7-6) emission. The data points with filled circles and labels of source names are from Tables 1 and 2 in the present paper. Other data points are from Blake et al. (1995), Moriarty-Schieven et al. (1994, 1995b), and Froebrich (2005). A bold line shows the result of the linear fitting to all the data points.

position along $R.A.$ and $Decl.$, v_0 is the central velocity of the spectrum toward the central protostellar position, or the systemic velocity, and a and b are the velocity gradients along $R.A.$ and $Decl.$, respectively. In the case of L483 and B335 the outflow axes are along the $R.A.$ direction, and hence a and b denote the velocity gradients along and across the outflow direction, respectively. In the case of L1551 IRS 5 we rotated the vector (a, b) by -18° to estimate the velocity gradients along and across the outflow axis. These fittings enable us to estimate the velocity gradients and the statistical errors along and across the outflow direction unambiguously. Figures 18, 19, 20, 21, and 22 show the results of the Gaussian fittings to the CS and HCN spectra in L1551 IRS 5, CS and HCN spectra in L483, and the CS spectra in B335, respectively. Table 3 summarizes the results of the plane fittings.

Figure 18 shows that the CS spectra in L1551 IRS 5 at the north-eastern side are blueshifted whereas those at the south-western side redshifted. This sense of the velocity gradient is opposite to the sense of the infalling envelope and the associated outflow. The estimated velocity gradient along the outflow direction is $\sim(-9.7 \pm 1.7) \times 10^{-3} \text{ km s}^{-1} \text{ arcsec}^{-1}$ (here the negative sign denotes the opposite velocity gradient to that of the associated outflow

and the millimeter molecular lines). The derived velocity gradient is ~ 5.9 times the statistical error, and hence the presence of the velocity gradient in the CS emission opposite to that of the millimeter lines and the outflow is statistically significant. In L483, Figure 20 shows that the CS emission tends to be blueshifted at the eastern side and redshifted at the western side. The estimated value of the velocity gradient along the outflow direction is $(-7.6 \pm 2.4) \times 10^{-3} \text{ km s}^{-1} \text{ arcsec}^{-1}$, ~ 3.2 times the statistical error. No statistical significance of the opposite velocity gradient in the CS (7–6) emission was obtained in B335.

Contrary to the CS (7–6) emission, no significant velocity gradient along any direction was verified in the HCN (4–3) emission (Table 3). One possible interpretation of the absence of the velocity gradients in the HCN (4–3) emission is the blending from the hyperfine components. As already mentioned in §3.1., two of the six hyperfine components, $F = 3-3$ and $F = 4-4$, are shifted by -1.67 km s^{-1} and 1.36 km s^{-1} from the main component ($F = 4-3$), respectively. The typical line widths measured from the CS (7–6) line in those protostellar envelopes are 1 - 2 km s^{-1} , and hence the $F = 3-3$ and $F = 4-4$ hyperfine components could totally smear the velocity gradient in the main $F = 4-3$ component if the intensity of those satellite lines are comparable to that of the main line. The much broader HCN line widths than the CS line widths found in L483 and L723 could also be due to the presence of the hyperfine lines.

From these statistical analyses, we suggest that at least the CS (7–6) line in L1551 IRS 5 and L483 shows opposite velocity gradients to those of the millimeter lines and the associated outflows. It is therefore intriguing to discuss the origin of these opposite velocity gradients in the submillimeter line. As discussed in the last subsection the submillimeter molecular emission likely traces the warm surface of the cavity opened by the outflow in the envelope, whereas the millimeter emission the colder, infalling region at the midplane. Therefore, the submillimeter molecular line should trace a distinct gas motion at the cavity wall in the envelopes. A possible interpretation of the observed velocity structures seen in the submillimeter line is an expanding gas motion which is perpendicular to the outflow axis. The surface of the cavity wall in the envelope traced by the submillimeter emission could be stripped away by some mechanism such as the stellar wind. As shown in Figure 15, on the side of the blueshifted outflow the bulk of the expanding gas at the cavity wall must be observed as a redshifted component and on the side of the redshifted outflow as a blueshifted component. On the other hand, the infalling gas component shows the same velocity gradient as that of the outflow. Hence, this configuration could explain the opposite velocity gradient observed in the submillimeter line to that of the outflow or infalling gas traced by the millimeter lines. In L1551 IRS 5, Pyo et al. (2005) have observed low-velocity ($\sim 100 \text{ km s}^{-1}$) [Fe II] winds with a wide opening angle of $\sim 100^\circ$, as well as collimated high-velocity ($\sim 300 \text{ km s}^{-1}$) jets along the polar axis. They have suggested that such a wind with a wide opening angle will be effective in sweeping up envelope material from the close vicinity of its driving source. The observed velocity structure of the submillimeter CS line in L1551 IRS 5 may trace such a gas motion in the envelope, although the spatial scale in

Table 3. Results of the plane fitting to the centroid velocities of the submillimeter spectra

Line	Source	a^* $\times 10^{-3}$ (km s $^{-1}$ arcsec $^{-1}$)	b^\dagger $\times 10^{-3}$ (km s $^{-1}$ arcsec $^{-1}$)	v_0^\ddagger (km s $^{-1}$)	rms^\S (km s $^{-1}$)
CS ($J=7-6$)	L1551 IRS 5	-9.7 \pm 1.7	-3.6 \pm 1.4	6.51 \pm 0.03	0.14
	L483	-7.6 \pm 2.4	3.6 \pm 2.8	5.52 \pm 0.05	0.14
	B335	-6.5 \pm 5.8	-3.1 \pm 6.5	8.18 \pm 0.06	0.07
HCN ($J=4-3$)	L1551 IRS 5	1.2 \pm 1.7	6.1 \pm 2.1	6.34 \pm 0.04	0.09
	L483	1.4 \pm 3.4	8.5 \pm 3.4	5.62 \pm 0.14	0.06

*Velocity gradient along the outflow direction. The negative sign denotes the opposite velocity gradient to that of the associated outflow.

† Velocity gradient across the outflow direction. The negative sign denotes the opposite velocity gradient to that of millimeter molecular lines.

‡ Systemic velocity measured from the one-component Gaussian fitting to the spectrum toward the protostellar position.

§ Rms of the plane fitting to the centroid velocities measured from the Gaussian fitting to the spectra.

our observations (\sim 2500 AU) is much larger than that of the [Fe II] observations (\sim 100 - 400 AU).

On the other hand, previous SMA observations of protostellar envelopes in submillimeter molecular lines have found compact (\lesssim 500 AU) components associated with the central protostars, and those components show mainly rotational gas motion around the protostars (Takakuwa et al. 2004; Takakuwa et al. 2007b; Brinch et al. 2007; Lommen et al. 2008; Jørgensen et al. 2009; Yen, Takakuwa, & Ohashi 2011). As already mentioned in the last subsection, our combined ASTE + SMA images of the protostellar envelopes around L1551 IRS 5 and B335 clearly show both the compact components and the extended components tracing the reflection nebulae. These results suggest that there are two distinct submillimeter components around protostellar sources; one is a compact (\lesssim 500 AU), rotating gas component in the vicinity of the central protostars, and the other extended (\sim 2000 AU) feature probably tracing the warm cavity wall of the envelope irradiated by the central protostars.

5. Summary

We have conducted mapping observations of L1551 IRS 5, L1551 NE, L723, and L43, and single-point observations of IRAS 16293-2422 in the submillimeter CS ($J = 7-6$) and HCN ($J = 4-3$) lines with ASTE. We have analyzed the present new ASTE data as well as our previous ASTE data of L483, B335, L723, and IRAS 16293-2422 (Paper I) in a systematical way, and have obtained the following results.

- 1 We detected the CS and HCN lines toward all the protostellar positions above 4σ level, except for the CS and HCN lines at the protostellar position of L1551 NE and the CS line at the protostellar position of L43. The CS intensity ranges from \lesssim 0.5 K (L1551 NE) to

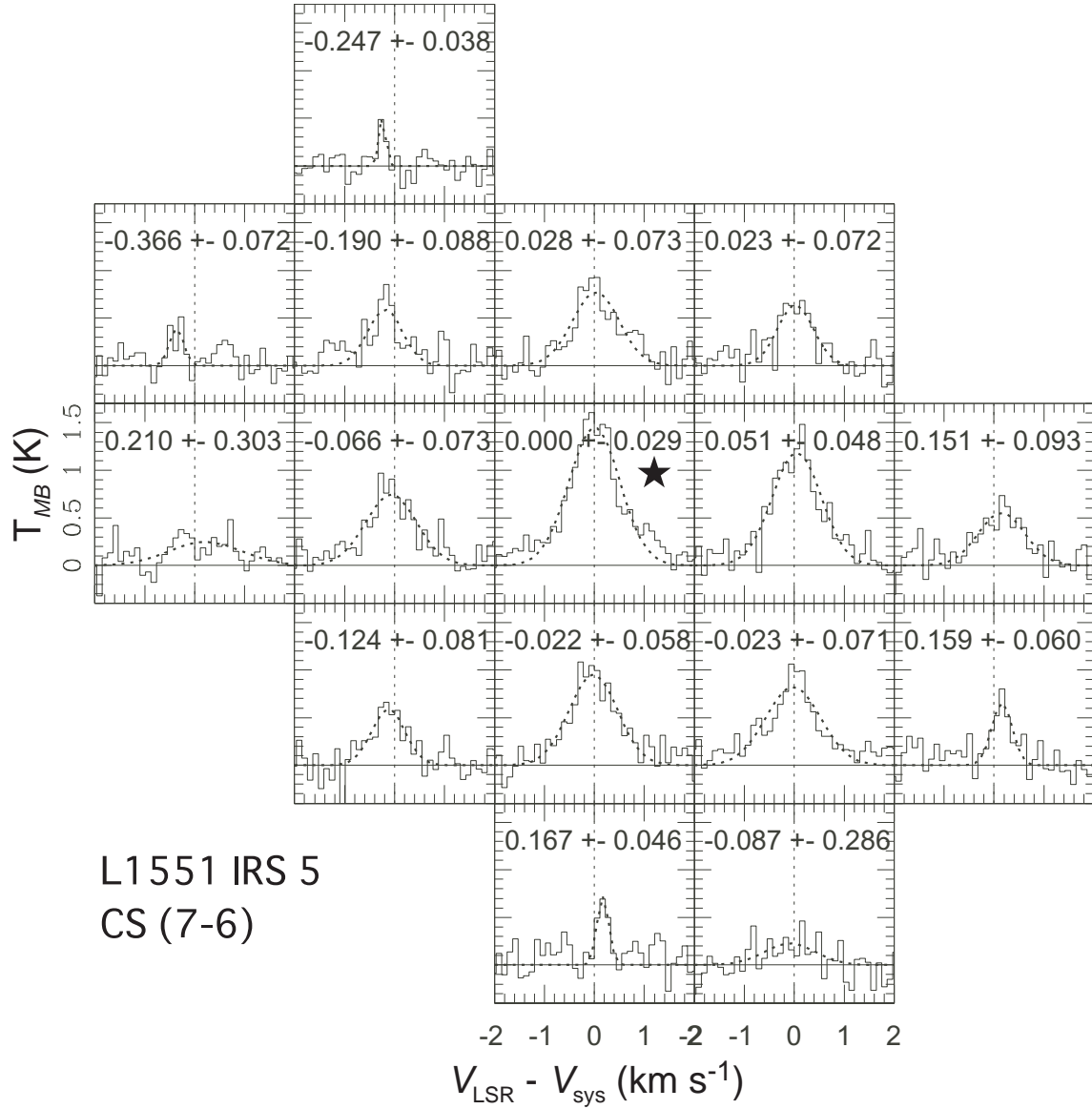


Fig. 18. Result of the Gaussian fitting to the CS (7-6) spectra in L1551 IRS 5 to derive the distribution of the centroid velocity. Histograms show the observed line profiles, while dashed curves fitted Gaussians. The horizontal axis shows the relative velocities with respect to the systemic velocity (vertical dashed lines) measured toward the protostellar position (star mark). Horizontal solid lines show the zero intensity level, and the derived relative velocity is shown in each panel. The grid spacing is $10''$, and the upper side is north and the right west.

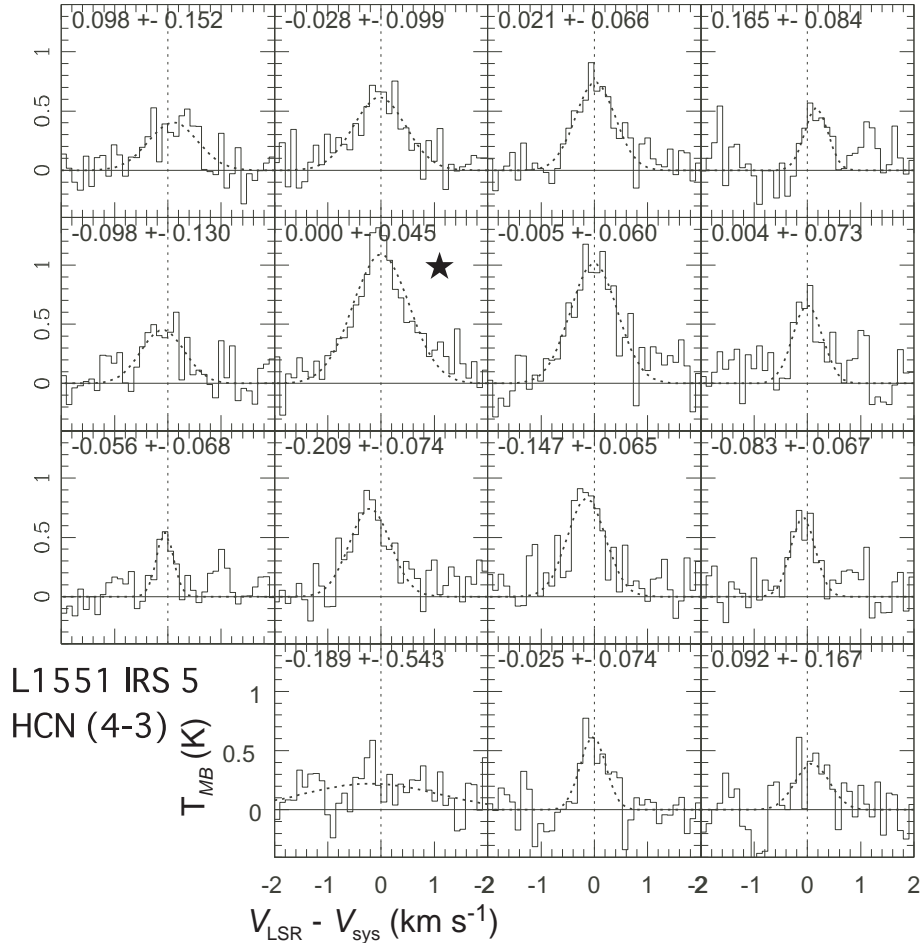


Fig. 19. Same as Figure 18 but for the HCN (4-3) emission.

~ 9.1 K (IRAS 16293-2422), and the HCN intensity from ~ 0.4 K (L723) to ~ 5.8 K (IRAS 16293-2422). The CS line is stronger than the HCN line toward all the sources except for L43. There is a linear correlation between the source luminosities and the intensities of these submillimeter lines ($I_{CS} \propto L_{bol}^{0.92}$).

- 2 Our mapping observations of the protostellar envelopes in the CS and HCN emissions show that the submillimeter emissions often exhibit “skewed” distributions toward the direction of the associated reflection nebulae. In the combined ASTE + SMA CS (7-6) image of L1551 IRS 5 there appears an extended (~ 2000 AU) component tracing the associated reflection nebula at the southwest, as well as a compact ($\lesssim 500$ AU) component centered on the protostellar position. The peaks of the CS and HCN emissions in L1551 NE are not located at the protostellar position but offset by ~ 1400 AU toward the west, where the associated reflection nebula resides. The CS emission in L723 is also skewed toward the direction of the blueshifted outflow. These results are consistent with our earlier result in L483, where the CS and HCN emissions are resolved and show elongation (> 2000 AU) toward the direction of the associated reflection nebula (Paper I). We suggest that these

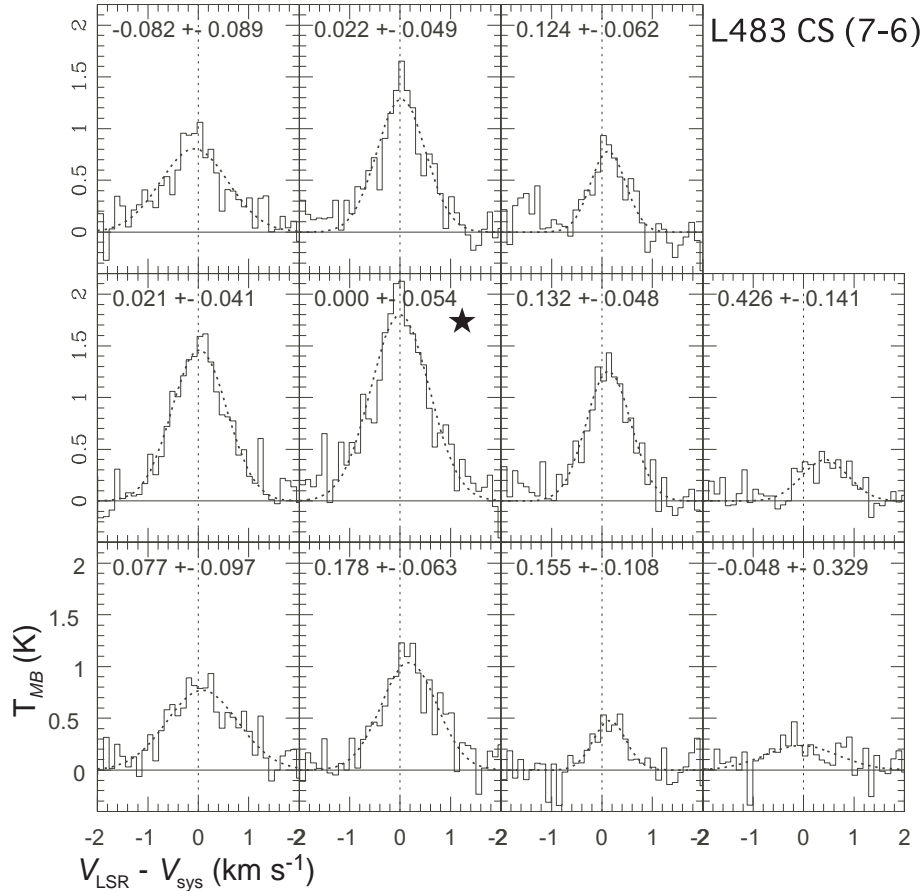


Fig. 20. Same as Figure 18 but for L483.

skewed submillimeter molecular emissions at a few thousands AU scale trace the warm ($\gtrsim 40$ K) walls of the envelope cavities, excavated by the associated blueshifted outflows and irradiated by the central protostars directly. On the other hand, the submillimeter emissions at the other side are obscured due to the absorption from the cold (~ 10 K) and dense ($\sim 10^6$ cm $^{-3}$) foreground envelope material. The detected linear correlation between the protostellar luminosities and the intensities of the submillimeter molecular lines may also support this interpretation.

- 3 From our statistical analyses, we verified that along the outflow directions the CS (7–6) emission in L1551 IRS 5 and L483 shows opposite velocity gradients to those of the millimeter molecular emissions and the associated outflows. The velocity gradients are estimated to be $(9.7 \pm 1.7) \times 10^{-3}$ km s $^{-1}$ arcsec $^{-1}$ in L1551 IRS 5 and $(7.6 \pm 2.4) \times 10^{-3}$ km s $^{-1}$ arcsec $^{-1}$ in L483. One possible interpretation on the origin of the different velocity gradients is that the submillimeter molecular line traces the dispersing gas motion at the surface of the cavity opened by the outflow in the envelope, which is perpendicular to the outflow direction. The absence of any clear velocity gradient in the HCN (4–3) emission may be due to the presence of the hyperfine components and the blending of the

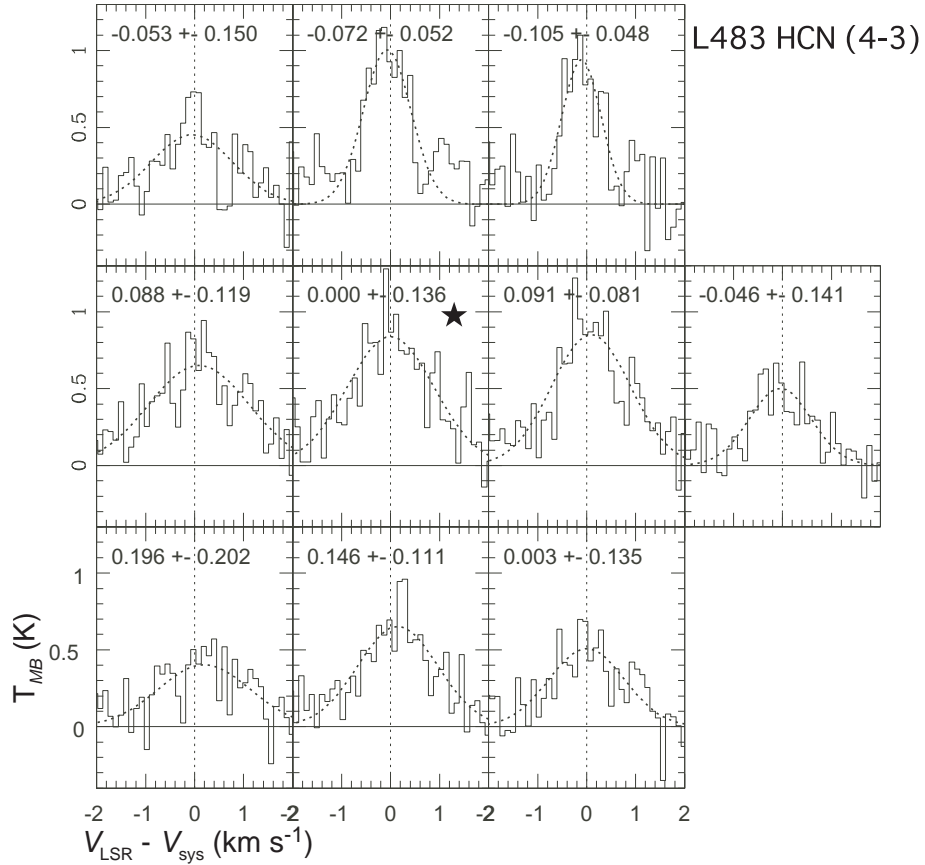


Fig. 21. Same as Figure 20 but for the HCN (4-3) emission.

velocity features.

We are grateful to N. Ohashi, P. T. P. Ho, and Masao Saito for their fruitful discussions. We thank all the ASTE staff for their dedicated support of the telescope and observatory operations. Observations with ASTE were carried out remotely from Japan by using NTT's GEMnet2 and its partner R&E (Research and Education) networks, which are based on AccessNova collaboration of University of Chile, NTT Laboratories, and National Astronomical Observatory of Japan. A part of this study was financially supported by the MEXT Grant-in-Aid for Scientific Research on Priority Areas No. 15071202. S. T. acknowledges the grant from the National Science Council of Taiwan (NSC 99-2112-M-001-009-MY3) in support of this work.

References

- André, P., Ward-Thompson, D., & Barsony, M. 2000, in *Protostars and Planets IV*, ed. V. Mannings, A. P. Boss, & S. S. Russell (Tucson, AZ: Univ. of Arizona Press), 59
- Anglada, G., Estalella, R., Rodríguez, L. F., Torrelles, J. M., López, R., & Cantó, J. 1991, *ApJ*, 376, 615

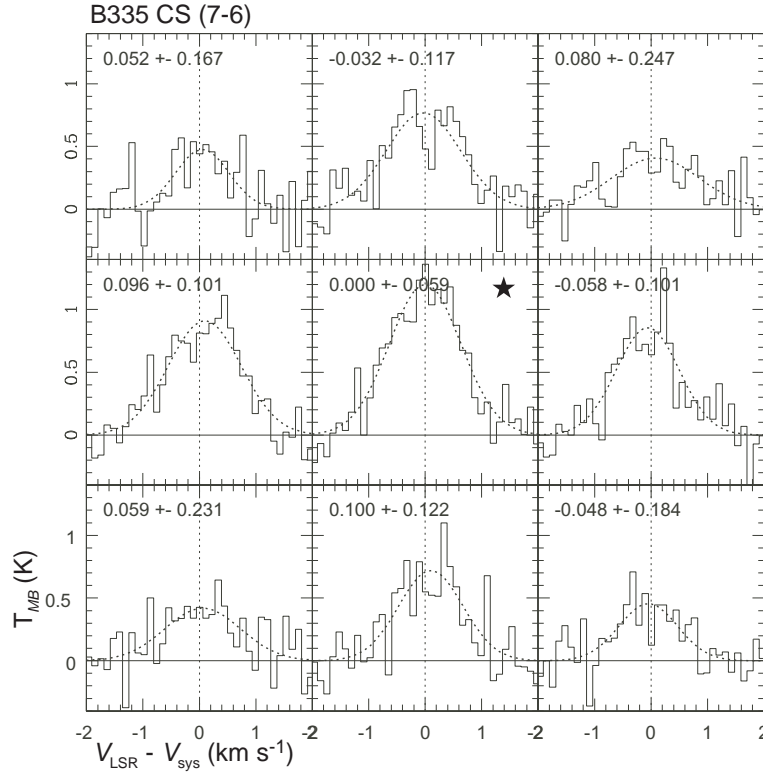


Fig. 22. Same as Figure 18 but for B335.

- Anglada, G., & Rodríguez, L. F. 2002, *RMxAA*, 38, 13
- Bence, S. J., Padman, R., Isaak, K. G., Wiedner, M. C., & Wright, G. S. 1998, *MNRAS*, 299, 965
- Blake, G. A., van Dishoeck, E. F., Jansen, D. J., Groesbeck, T. D., & Mundy, L. G. 1994, *ApJ*, 428, 680
- Blake, G. A., Sandell, G., van Dishoeck, E. F., Groesbeck, T. D., Mundy, L. G., & Aspin, C. 1995, *ApJ*, 441, 689
- Brinch, C., Crapsi, A., Jørgensen, J. K., Hogerheijde, M. R., & Hill, T. 2007, *A&A*, 475, 915
- Carrasco-González, C., Anglada, G., Rodríguez, L. F., Torrelles, J. M., Osorio, M., & Girart, J. M. 2008, *ApJ*, 676, 1073
- Chen, J.-H., Evans, N. J., Lee, J.-E., & Bourke, T. L. 2009, *ApJ*, 705, 1160
- Chin, Y.-N., Henkel, C., Whiteoak, J. B., Langer, N., & Churchwell, E. B. 1996, *A&A*, 305, 960
- Davidson, J. A. 1987, *ApJ*, 315, 602
- Devine, D., Reipurth, B., & Bally, J. 1999, *ApJ*, 118, 972
- Draper, P. W., Warren-Smith, R. F., & Scarrott, S., M. 1985, *MNRAS*, 216, 7
- Emerson, J. P., Harris, S., Jennings, R. E., Beichman, C. A., Baud, B., Beintema, D. A., Marsden, P. L., Wesselius, P. R. 1984, *ApJL*, 278, L49
- Ezawa, H., Kawabe, R., Kohno, K., & Yamamoto, S. 2004, *Proc. SPIE*, 5489, 763
- Froebrich D. 2005, *ApJS*, 156, 169
- Girart, J. M., Rao, R., & Estalella, R. 2009, *ApJ*, 694, 56
- Goldreich, P., & Kwan, J. 1974, *ApJ*, 189, 441

- Goodman, A. A., Benson, P. J., Fuller, G. A., & Myers, P. C. 1993, *ApJ*, 406, 528
- Gregersen, E. M., Evans II, N. J., Zhou, S., & Choi, M. 1997, *ApJ*, 484, 256
- Hayashi, S. S., Hasegawa, T., & Kaifu, N. 1991, *ApJ*, 377, 492
- Hayashi, M., & Pyo, T.-S. 2009, *ApJ*, 694, 582
- Hirano, N., Hayashi, S. S., Umemoto, T., & Ukita, N. 1998, *ApJ*, 504, 334
- Hodapp, K.-W., & Ladd, E. F. 1995, *ApJ*, 453, 715
- Jewitt, D. C., Matthews, H. E., Owen, T., & Meier, R. 1997, *Science*, 278, 90
- Jørgensen, J. K., van Dishoeck, E. F., Visser, R., Bourke, T. L., Wilner, D. J., Lommen, D., Hogerheijde, M. R., & Myers, P. C. 2009, *A&A*, 507, 861
- Kamazaki, T., et al. 2005, *Astronomical Society of the Pacific Conference Series*, 347, 533
- Kohno, K. 2005, in *ASP Conf. Ser. 344, The Cool Universe: Observing Cosmic Dawn*, ed C. Lidman & D. Alloin, (San Francisco: ASP), 242
- Landman, D. A., Roussel-Dupre, R., & Tanigawa, G. 1982, *ApJ*, 261, 732
- Lee, C.-F., Mundy, L. G., Reipurth, B., Ostriker, E. C., & Stone, J. M. 2000, *ApJ*, 542, 925
- Lee, C.-F., Mundy, L. G., Stone, J. M., & Ostriker, E. C. 2002, *ApJ*, 576, 294
- Lim, J., & Takakuwa, S. 2006, *ApJ*, 653, 425
- Lommen, D., Jørgensen, J. K., van Dishoeck, E. F., & Crapsi, A. 2008, *A&A*, 481, 141
- Momose, M., Ohashi, N., Kawabe, R., Nakano, T., & Hayashi, M. 1998, *ApJ*, 504, 314
- Moriarty-Schieven, G. H., Wannier, P. G., Keene, J., & Tamura, M. 1994, *ApJ*, 436, 800
- Moriarty-Schieven, G. H., Butner, H. M., & Wannier, P. G. 1995, *ApJL*, 445, L55
- Moriarty-Schieven, G. H., Wannier, P. G., Mangum, J. G., Tamura, M., & Olmsted, V. K. 1995, *ApJ*, 455, 190
- Moriarty-Schieven, G. H., Powers, J. A., Butner, H. M., Wannier, P. G., & Keene, J. 2000, *ApJL*, 533, L143
- Moriarty-Schieven, G. H., Johnstone, D., Bally, J., & Jenness, T. 2006, *ApJ*, 645, 357
- Myers, P. C., Evans, N. J., II, & Ohashi, N. 2000, in *Protostars and Planets IV*, ed. V. Mannings, A. P. Boss, & S. S. Russel (Tucson, AZ: Univ. of Arizona Press), 217
- Nakazato, T., Nakamoto, T., & Umemura, M. 2003, *ApJ*, 583, 322
- Ohashi, N., Hayashi, M., Ho, P. T. P., Momose, M., & Hirano, N. 1996, *ApJ*, 466, 957
- Ohashi, N., Hayashi, M., Ho, P. T. P., & Momose, M. 1997a, *ApJ*, 475, 211
- Ohashi, N., Hayashi, M., Ho, P. T. P., Momose, M., Tamura, M., Hirano, N., & Sargent, A. I. 1997b, *ApJ*, 488, 317
- Park, Y.-S., Panis, J.-F., Ohashi, N., Choi, M., & Minh, Y. C. 2000, *ApJ*, 542, 344
- Plambeck, P. L. & Snell, R. L. 1995, *ApJ*, 446, 234
- Pyo, T.-S., Hayashi, M., Kobayashi, N., Tokunaga, A. T., Terada, H., Tsujimoto, M., Hayashi, S. S., Usuda, T., Yamashita, T., Takami, H., Takato, N., & Nedachi, K. 2005, *ApJ*, 618, 817
- Reipurth, B., Yu, K. C., Heathcote, S., Bally, J., & Fodríguez, L. F. 2000, *ApJ*, 120, 1449
- Reipurth, B., Rodríguez, L. F., Anglada, & G., Bally, J. 2002, *ApJ*, 124, 1045
- Rodríguez, L. F., Anglada, G., & Raga, A. 1995, *ApJL*, 454, L149
- Saito, M., Kawabe, R., Kitamura, Y., & Sunada, K. 1996, *ApJ*, 473, 464
- Saito, M., Kawabe, R., Kitamura, Y., & Sunada, K. 2001, *ApJ*, 547, 840

Scoville, N. Z., & Solomon, P. M. 1974, ApJL, 187, L67
Shirley, Y. L., Evans II, N. J., Rawlings, J. M. C., & Gregersen, E. M. 2000, ApJS, 131, 249
Snell, R. L., Loren, R. B., & Plambeck, R. L. 1980, ApJ, 239, 17
Spaans, M., Hogerheijde, M. R., Mundy, L. G., & Van Dishoeck, E. F. 1995, ApJL, 455, L167
Stojimirović, I., Narayanan, G., Snell, R. L., Bally, J. 2006, ApJ, 649, 280
Takakuwa, S., Mikami, H., Saito, M., & Hirano, N. 2000, ApJ, 542, 367
Takakuwa, S., Ohashi, N., Ho, P. T. P., Chunhua, Q., Wilner, D. J., Qizhou, Z., Bourke, T. L., Hirano, N., Choi, M., & Yang, J. 2004, ApJL, 616, L15
Takakuwa, S., Kamazaki, T., Saito, M., Yamaguchi, N., & Kohno, K. 2007a, PASJ, 59, 1 (Paper I)
Takakuwa, S., et al. 2007b, ApJ, 662, 431
Uchida, Y., Kaifu, N., Shibata, K., Hayashi, S. S., Hasegawa, T., & Hamatake, H. 1987, PASJ, 39, 907
van Dishoeck, E. F., Blake, G. A., Jansen, D. J., & Groesbeck, T. D. 1995, ApJ, 447, 760
Whitney, B. A., Wood, K., Bjorkman, J. E., & Wolff, M. J. 2003, ApJ, 591, 1049
Wu, P.-F., Takakuwa, S., & Lim, J. 2009, ApJ, 698, 184
Yen, H.-W., Takakuwa, S., & Ohashi, N. 2010, ApJ, 710, 1786
Yen, H.-W., Takakuwa, S., & Ohashi, N. 2011, ApJ, submitted
Yokogawa, S., Kitamura, Y., Momose, M., & Kawabe, R. 2003, ApJ, 595, 266